6-2-2015

GPS Phase Scintillation at High Latitudes during Geomagnetic Storms of 7–17 March 2012 – Part 1: The North American Sector

P. Prikryl
University of New Brunswick

R. Ghoddousi-Fard
Natural Resources Canada

E. G. Thomas
Virginia Polytechnic Institute and State University

J. M. Ruohoniemi
Virginia Polytechnic Institute and State University

S. G. Shepherd
Dartmouth College

Ann. Geophys., 33, 637–656, 2015
www.ann-geophys.net/33/637/2015/
doi:10.5194/angeo-33-637-2015

Annales Geophysicae
Open Access

GPS phase scintillation at high latitudes during geomagnetic storms of 7–17 March 2012 – Part 1: The North American sector

P. Prikryl[1,5], R. Ghoddousi-Fard[2], E. G. Thomas[3], J. M. Ruohoniemi[3], S. G. Shepherd[4], P. T. Jayachandran[5], D. W. Danskin[1], E. Spanswick[6], Y. Zhang[7], Y. Jiao[8], and Y. T. Morton[8]

[1]Geomagnetic Laboratory, Natural Resources Canada, Ottawa, ON, Canada
[2]Canadian Geodetic Survey, Natural Resources Canada, Ottawa, ON, Canada
[3]Bradley Department of Electrical and Computer Engineering, Virginia Tech, Blacksburg, VA, USA
[4]Thayer School of Engineering, Dartmouth College, Hanover, NH, USA
[5]Physics Department, University of New Brunswick, Fredericton, NB, Canada
[6]Department of Physics and Astronomy, University of Calgary, Calgary, AB, Canada
[7]Johns Hopkins University Applied Physics Lab, Laurel, MD, USA
[8]Department of Electrical and Computer Engineering, Colorado State University, Fort Collins, CO, USA

Correspondence to: P. Prikryl (paul.prikryl@unb.ca)

Received: 18 December 2014 – Revised: 1 April 2015 – Accepted: 4 May 2015 – Published: 2 June 2015

Abstract. The interval of geomagnetic storms of 7–17 March 2012 was selected at the Climate and Weather of the Sun-Earth System (CAWSES) II Workshop for group study of space weather effects during the ascending phase of solar cycle 24 (Tsurutani et al., 2014). The high-latitude ionospheric response to a series of storms is studied using arrays of GPS receivers, HF radars, ionosondes, riometers, magnetometers, and auroral imagers focusing on GPS phase scintillation. Four geomagnetic storms showed varied responses to solar wind conditions characterized by the interplanetary magnetic field (IMF) and solar wind dynamic pressure. As a function of magnetic latitude and magnetic local time, regions of enhanced scintillation are identified in the context of coupling processes between the solar wind and the magnetosphere–ionosphere system. Large southward IMF and high solar wind dynamic pressure resulted in the strongest scintillation in the nightside auroral oval. Scintillation occurrence was correlated with ground magnetic field perturbations and riometer absorption enhancements, and collocated with mapped auroral emission. During periods of southward IMF, scintillation was also collocated with ionospheric convection in the expanded dawn and dusk cells, with the antisunward convection in the polar cap and with a tongue of ionization fractured into patches. In contrast, large northward IMF combined with a strong solar wind dynamic pressure pulse was followed by scintillation caused by transpolar arcs in the polar cap.

Keywords. Ionosphere (ionospheric disturbances; ionospheric irregularities; polar ionosphere)

1 Introduction

Space weather impacts the operation of modern technology that relies on global navigation satellite systems (GNSS). Ionospheric scintillation (rapid fluctuation of radio wave amplitude and phase) degrades GPS positional accuracy and causes cycle slips, leading to a loss of lock that affects the performance of radio communication and navigation systems (Aquino et al., 2007; Kintner et al., 2007), sometimes even during an insignificant storm (Andalsvik and Jacobsen, 2014). At high latitudes, the occurrence of ionospheric scintillation is largely determined by solar wind disturbances coupling to the magnetosphere–ionosphere system, resulting in steep electron density gradients and irregularities. The main ionospheric regions that are affected by scintillation are the nightside auroral oval, the cusp/cleft on the dayside and the polar cap (Aarons, 1997; Aarons et al., 2000; Basu et al., 1987, 1995, 1998; Spogli et al., 2009; Tiwari et al., 2010; Prikryl et al., 2011; Moen et al., 2013; van der Meeren et al., 2014). However, moderately strong scintillation can also

occur at subauroral latitudes. At auroral latitudes, the ionosphere is structured by energetic particle precipitation, particularly during auroral substorms, when scintillation is often located with bright auroras (Kinrade et al., 2013; Prikryl et al., 2013a, b). In the ionospheric footprint of the magnetospheric cusp, fast-drifting irregularities and steep density gradients at the edges of electron density depletions carved by intense flow channels that are signatures of magnetic reconnection at the dayside magnetopause (Pinnock et al., 1993; Prikryl et al., 1999; Carlson, 2012) are likely causes of scintillation. Dense ionospheric plasma, a tongue of ionization (TOI), is drawn from the dayside midlatitudes to polar cap through the cusp, where it is segmented into patches. The patches convect across the polar cap, often at high speed, causing scintillation. At subauroral latitudes, density gradients and irregularities within subauroral polarization streams (SAPSs) and storm-enhanced densities (SEDs) (Foster, 1993; Foster and Burke, 2002; Clausen et al., 2012; Kunduri et al., 2012) can also result in scintillation of GNSS signals (Prikryl et al., 2013b).

Geomagnetic storms provide opportunities to study the dynamics of ionospheric phenomena in the context of coupling processes between solar wind and the magnetosphere–ionosphere system and to map scintillation occurrence as a function of magnetic latitude, local time, and solar wind conditions, in particular the interplanetary magnetic field (IMF). Recently, this has become possible because of improved coverage at high latitudes by high-rate GPS receivers to monitor scintillation. Understanding such dependencies will enable us to predict scintillation occurrence and mitigate detrimental effects on communication and navigation technologies.

Interplanetary coronal mass ejections (ICMEs) and corotating interaction regions on the leading edge of high-speed streams (HSSs) are the most geo-effective solar wind disturbances that impact the ionosphere and result in scintillation of transionospheric radio signals. The period of 7–17 March 2012 was selected by the CAWSES-II Workshop for an intensive group study of various facets of space weather features that occurred during the first major geomagnetically active interval of the ascending phase of solar cycle 24. Tsurutani et al. (2013) provided an overview of major solar, interplanetary, magnetospheric, and ionospheric features of this interval and suggested space weather topics of interest that require further study. The purpose of the present paper is to complement the abovementioned study and investigate the high-latitude ionosphere response to variable solar wind conditions focusing on GNSS phase scintillation in the North American sector. While statistical studies have identified main regions where scintillation occurs, we still have limited knowledge of what specific solar wind conditions and ionospheric structures result in scintillation and at what altitudes. Through combination of observations of phase scintillation obtained by a high-rate scintillation receiver array with a proxy phase scintillation index derived from differential phase measurements by many 1 Hz receivers, we now have tools to map scintillation with sufficient detail to be compared with maps of ionospheric convection, auroral emission, and TEC. Such comparisons aim at addressing questions where, when and under what solar wind conditions and in what ionospheric structure does scintillation occur at high latitudes, and thus lead to better understanding of the physical processes that cause scintillation. In a companion paper (Prikryl et al., 2015a), this study is extended to southern high latitudes to examine interhemispheric asymmetries.

2 Instruments and data

The Canadian High Arctic Ionospheric Network (CHAIN) (Jayachandran et al., 2009) consists of GPS ionospheric scintillation and TEC monitors (GISTMs) and Canadian advanced digital ionosondes (CADIs). It is complemented by an array of geodetic quality GPS receivers recording at a sampling rate of 1 Hz (Fig. 1). The GISTM receiver is a GSV 4004B model (Van Dierendonck and Arbesser-Rastburg, 2004), which is a NovAtel OEM4 dual-frequency receiver with special firmware specifically configured to measure and record power and phase of the GPS L1 signal at a high sampling rate (50 Hz). Each receiver is capable of tracking and reporting scintillation and total electron content (TEC) measurements simultaneously from up to 10 GPS satellites in view. The GSV 4004B can also automatically compute and record S_4 and σ_Φ indices. The phase scintillation index σ_Φ is the standard deviation of the detrended phase using a filter in the receiver with 0.1 Hz cutoff frequency. One-minute values of σ_Φ are used in this paper. CHAIN data are supplemented by scintillation data from the same type of receiver operated in Gakona, Alaska (Jiao et al., 2013).

GPS receivers with 1 Hz sampling rate in North America are used to complement the CHAIN stations' scintillation measurements by computing 30 s proxy indices (mean of the delta phase rate, mDPR, and standard deviation of the delta phase rate, sDPR) (Ghoddousi-Fard et al., 2013). In brief, these indices are based on the rate of the GPS dual-frequency carrier phase at two consecutive epochs 1 s apart expressed in units of millimeters per second. As shown by Ghoddousi-Fard et al. (2013), the sDPR index is well correlated with the phase scintillation index σ_Φ. Figure 1 shows the locations of GPS receivers in the North American sector. Receivers from other longitude sectors that are used for mapping scintillation are shown in a companion paper on interhemispheric comparison of phase scintillation (Prikryl et al., 2015a).

The GPS TEC maps are obtained using the plotting tools (Thomas et al., 2013) available online (http://vt.superdarn.org) with the TEC data downloaded from the Madrigal database (http://madrigal.haystack.mit.edu/madrigal/). The TEC data were processed using MIT Automated Processing of GPS (MAPGPS) software, which allows the processing of GPS data into global TEC maps (Rideout and Coster, 2006).

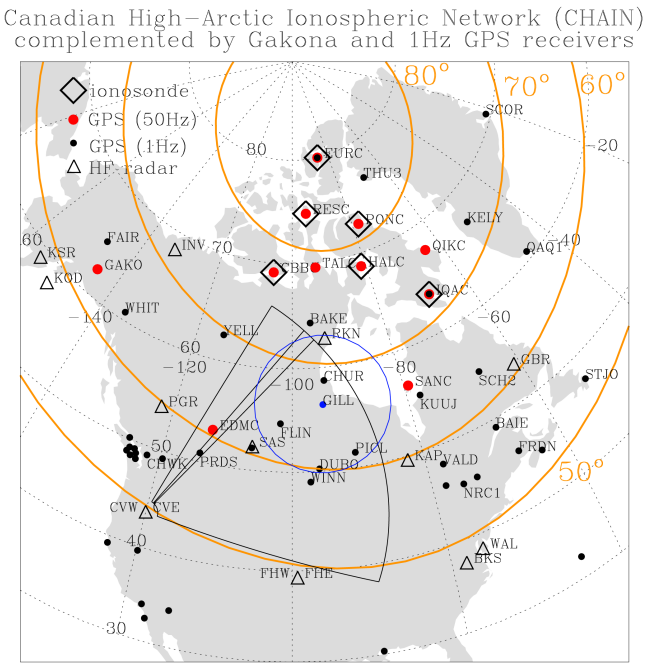

Figure 1. The GPS ionospheric scintillation and TEC monitors (red dots) complemented by geodetic-quality GPS receivers recording at sampling rate of 1 Hz (black dots). Fields of view of an all-sky imager (ASI) in Gillam and the SuperDARN Christmas Valley East radar are shown, with radar beam 3 highlighted. Locations of SuperDARN radars are indicated by triangles. The altitude-adjusted corrected geomagnetic (AACGM) latitudes 50, 60, 70, and 80°, in yellow, are superposed over the geographic grid.

Solar wind data were obtained from the Goddard Space Flight Center Space Physics Data Facility CDAWeb and OMNIWeb data sets (King and Papitashvili, 2005). The OMNIWeb data set of interplanetary magnetic field and solar wind plasma parameters have combined the data from available solar wind monitors, primarily from Advanced Composition Explorer (ACE). The OMNIWeb data set propagates the solar wind measurements to the nose of the Earth's bow shock to accommodate for propagation delays from the spacecraft.

The GISTM arrays are supported by radars, optical instruments, and magnetometers of the Canadian Geospace Monitoring (CGSM) program (Liu, 2005; Mann et al., 2008), including magnetometers operated by the NRCan Geomagnetic Laboratory (http://www.spaceweather.ca). The Northern Solar Terrestrial Array (NORSTAR) (Donovan et al., 2003) is an optical and radio facility designed to remotely sense auroral precipitation on a continental scale. NORSTAR consists of CCD-based all-sky imagers (ASIs), meridian-scanning photometers, and riometers.

Additionally, data from the Special Sensor Ultraviolet Scanning Imager (SSUSI) onboard the Defense Meteorological Satellite Program (DMSP) satellites (http://sd-www.jhuapl.edu/Aurora/) (F16 to F18) were used. SSUSI measures auroral and airglow emissions in FUV bands, and provides partial global auroral images in five "colors": 121.6 nm (proton aurora), 130.4 nm (O emission), 135.6 nm (O emission), 140 to 150 nm (Lyman–Birge–Hopfield (LBH)S: N2 LBH short band), and 165 to 180 nm (LBHL: N2 LBH long band) (Paxton et al. 2002). The LBHS and LBHL bands were used to derive the energy flux and mean energy of precipitating electrons in the auroral oval (Zhang and Paxton, 2008, and references therein). SSUSI takes 15 auroral images in both hemispheres every day, and the images have spatial resolution down to 10 km at nadir. The presented SSUSI auroral images have been re-binned with a grid side of 25 km × 25 km. The SSUSI is almost the same as a global ultraviolet imager (see Zhang and Paxton, 2008).

The Super Dual Auroral Radar Network (SuperDARN) is a network of coherent-backscatter HF radars with a collective field of view that covers a large fraction of the high-latitude ionosphere (Greenwald et al., 1995, Chisham et al., 2007). The radars transmit at frequencies 8–20 MHz along 16–24 contiguous, successively swept azimuthal beams, each of which is gated into 75–115 range bins. The bins are typically 45 km long in standard operations, and the dwell time for each beam is usually 3 or 7 s. A standard 16-beam scan with successive beams separated by 3.24° covers ∼52° in azimuth every 1 or 2 min. Several quantities including the line-of-sight Doppler velocity, spectral width, and backscatter power from field-aligned ionospheric plasma irregularities are routinely measured. The midlatitude component of SuperDARN has been expanded since 2009 owing to construction of several radars as part of the Mid-Sized Infrastructure (MSI) program (see, for example, Clausen et al., 2012). By the time the radar data that are presented in this paper were collected, the midlatitude SuperDARN coverage had reached across North America in an unbroken chain of interlocking radar fields of view. Figure 1 shows the field of view of the Christmas Valley East radar. Combined data from all Northern Hemisphere radars are used in the production of convection maps.

3 Summary of solar wind conditions and ionospheric/geomagnetic response during the 6–17 March 2012 interval

The overview paper by Tsurutani et al. (2014) has already provided some details on the interplanetary conditions as observed by the ACE spacecraft monitoring solar wind upstream from the Earth. In the present paper we will frequently refer to these eight authors (T8) for their findings, interpretations, and suggestions. A summary (Fig. 2a–e) of the solar wind OMNI data set projected to the subsolar bow shock shows 5 min averages of the solar wind velocity, V_{sw}; the IMF components B_y and B_z; total magnitude, B; and proton density, n_p. Figure 2g shows provisional geomagnetic indices AE and SYM-H. Five upstream interplanetary (IP) shocks that were identified by T8 are indicated by verti-

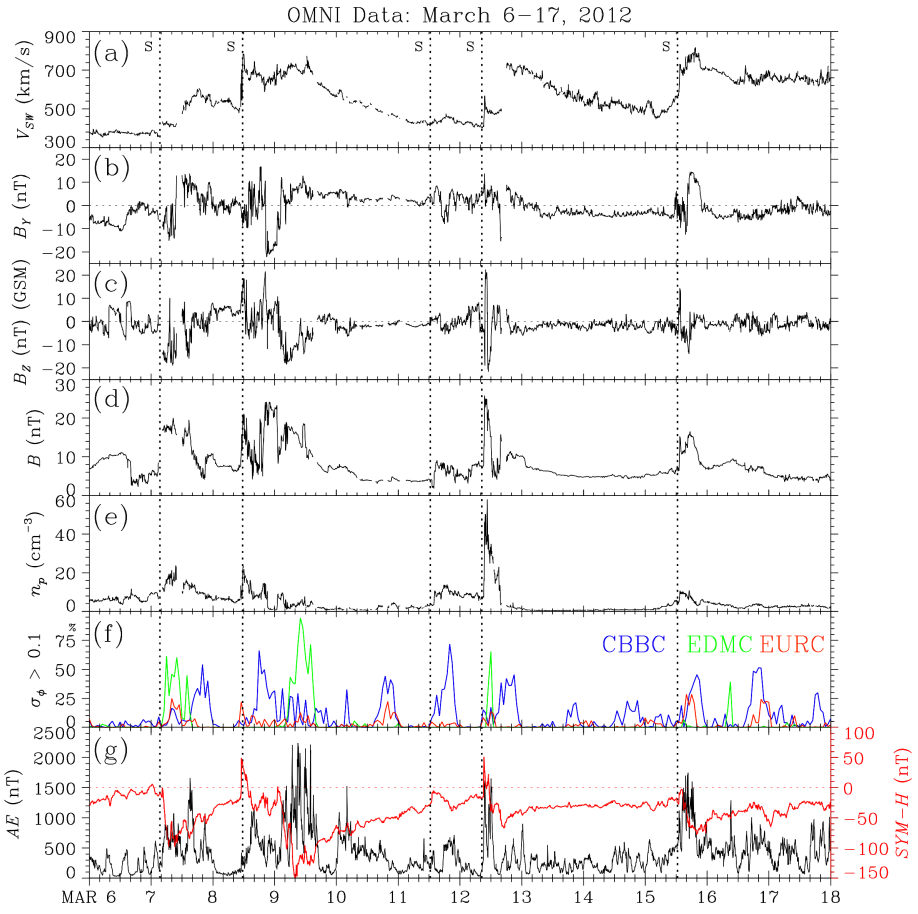

Figure 2. (a–e) The interplanetary data from the 5 min OMNI data set. **(f)** The hourly occurrences of phase scintillation ($\sigma_\Phi > 0.1$ rad) observed by CHAIN stations in Cambridge Bay (CBBC), Eureka (EURC), and Edmonton (EDMC), and **(g)** provisional geomagnetic indices AE and SYM-H.

cal dotted lines. It should be noted that the OMNI data are largely based on the data from the Wind spacecraft, which was unfavorably located far duskward of the Sun–Earth line ($Y_{GSE} \approx +90\ R_E$). The data from ACE that were located on the dawnside ($Y_{GSE} \approx -40\ R_E$) are shown by T8 and are used along with Geotail data for specific events in this paper. Four geomagnetic storms – S1, S2, S3 (a "double-shock" event), and S4 – that were discussed by T8 are characterized by deep depressions in the storm index SYM-H (Fig. 2g; red trace). The storms resulted in varied ionospheric responses that are discussed in more detail in Sects. 4–7. The AE index (Fig. 2g) peaked above 1500 nT during each of these storms, indicating intense auroral activity. The hourly occurrence of phase scintillation is shown in Fig. 2f for CHAIN stations at Eureka (EURC), Cambridge Bay (CBBC), and near Edmonton (EDMC), representing the central polar cap, cusp, and auroral/subauroral zone, respectively. The onsets of scintillation events were clearly linked to arrivals of IP shocks and onsets of geomagnetic storms, but the scintillation response clearly depended on latitude. The scintillation during storm S1 started in the auroral zone (EDMC) and was delayed in the polar cap (EURC). Just the opposite was the case during storm S2. The scintillation response following the first IP shock of storm S3 was limited to the cusp (CBBC), while there was no scintillation observed in EDMC and EURC. In contrast, the second IP shock triggered a prompt scintillation response at all latitudes. During storm S4, the scintillation occurred mostly in the cusp and polar cap. Of course, this variability can be partly attributed to local time of the IP shock arrival, but varied solar wind conditions such as the IMF orientation and dynamic pressure played a major role. This is addressed in Sects. 4–7.

Figures 3a and 4a show the phase scintillation occurrence as a function of altitude-adjusted corrected geomagnetic (AACGM) latitude (Baker and Wing, 1989; Shepherd, 2014) and universal time (UT). Using grid cells of 1° × 1 h in size, the percentage occurrence of $\sigma_\Phi > 0.1$ rad is shown. The mapping assumes IPP height of 350 km. To minimize the multipath effect, only satellite elevation angles exceeding 30° are used. The values of σ_Φ are projected to the vertical to account for geometrical effects on the measurements made at different elevation angles (Spogli et al., 2009; see

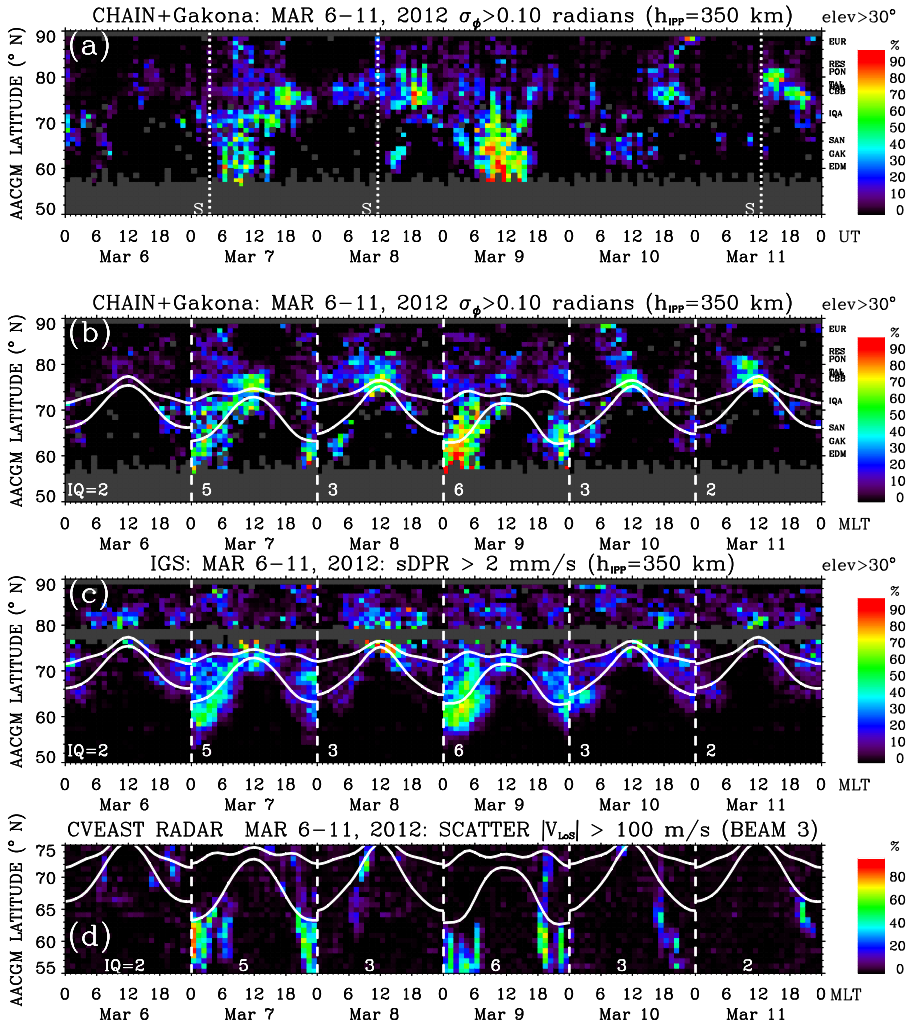

Figure 3. The occurrence of phase scintillation **(a, b)** $\sigma_\Phi > 0.1$ rad, **(c)** sDPR $> 2\,\mathrm{mm\,s^{-1}}$), and **(d)** Christmas Valley East radar backscatter ($V_{\mathrm{LOS}} > 100\,\mathrm{m\,s^{-1}}$) from 6 to 11 March. The maps are shown as a function of AACGM latitude and **(a)** UT or **(b–d)** MLT. The dotted vertical lines in the top panel indicate interplanetary shock arrival times in UT. The dashed vertical lines separate days mapped in MLT. The IQ value of the statistical auroral oval is chosen approximately proportional to a maximum 3-hourly Kp index.

their Eq. 1). The onsets of scintillation events, either in the cusp or at auroral/subauroral latitudes, closely followed the arrivals of upstream interplanetary shocks.

Figures 3b and 4b show the phase scintillation occurrence maps as a function of AACGM latitude and magnetic local time (MLT) computed for each day. The positions of the statistical auroral oval (Feldstein, 1967; Holzworth and Meng, 1975) are superposed in white solid lines. The control parameter for the Feldstein model is the index Q (IQ), ranging from 0 to 6 for a quiet to very active oval. It is shown for each day for conditions from IQ = 2 to IQ = 6, approximately proportional to a 3-hourly Kp index. The maps of $\sigma_\Phi > 0.1$ are supported by occurrence maps of the proxy phase scintillation index sDPR exceeding $2\,\mathrm{mm\,s^{-1}}$ (Figs. 3c and 4c) obtained for geodetic-quality receivers sampling at 1 Hz. There is a data gap at high latitudes, but the coverage at auroral and subauroral latitudes is good. In general, the sDPR maps show a scintillation occurrence that is very similar to phase scintillation $\sigma_\Phi > 0.1$ rad.

On each day, the phase scintillation occurrence was enhanced in the cusp and scintillation was extended into the polar cap. Figure 4b shows the clearest cases of scintillation bands indicating TOI or patches in the polar cap that are tilted toward the evening and morning hours on 15 and 16 March, when the IMF was predominantly duskward ($B_y > 0$) and dawnward ($B_y < 0$), respectively. Significantly enhanced scintillation also occurred at auroral and subauroral latitudes during the most disturbed days, particularly on 7, 9, 12, and 15 March.

The SuperDARN radars in Christmas Valley observed strong backscatter from fast convecting irregularities at auroral and subauroral latitudes. Figures 3d and 4d show the oc-

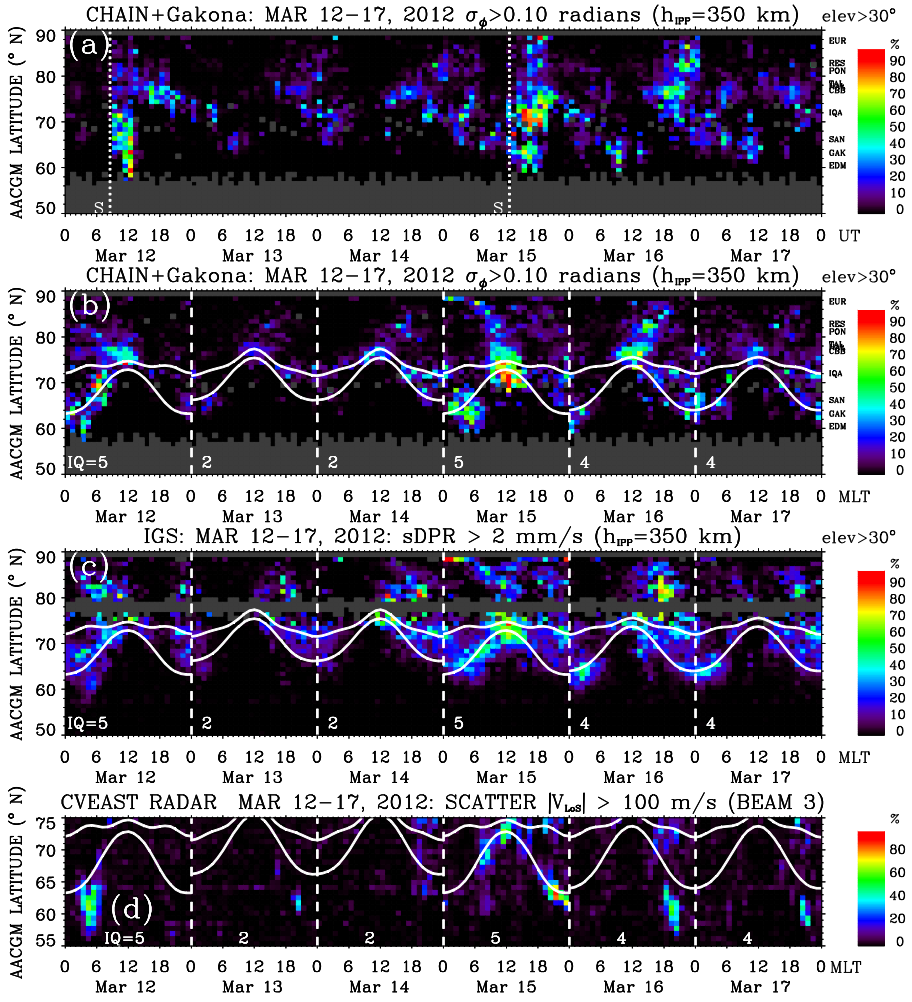

Figure 4. Same as Fig. 3 but for the time interval from 12 to 17 March.

currence of ionospheric backscatter from irregularities moving at line-of-sight velocity $V_{LOS} > 100\,m\,s^{-1}$ for beam 3 of the Christmas Valley East radar. Bands of high occurrence of auroral and subauroral backscatter after and before magnetic midnight approximately coincide with scintillation occurrence of $\sigma_\Phi > 0.1$ (Fig. 3d) and sDPR $> 2\,mm\,s^{-1}$ (Fig. 3c).

4 Event S1: 7 March 2012 – case of IMF $B_z < 0$

The IP shock at ∼ 03:30 UT was coincident with a strong southward IMF B_z (−17 nT) (Fig. 2c). It resulted in extensive auroral activity and a high occurrence of scintillation over a wide band of latitudes that continued for several hours (Fig. 3a). As discussed in more detail by T8, the intense southward IMF behind the IP shock, which was accompanied by enhancements in proton density and IMF magnitude, caused a rapid decrease in SYM-H to −98 nT, leading to a geomagnetic storm.

The IP shock was followed by an onset of phase scintillation at auroral latitudes at EDMC (Fig. 2f) that coincided with an increase in AE index (Fig. 2g). With a delay of a few hours, scintillation started in the polar cap (EURC), and after 16:00 UT in the cusp (CBBC) (see also Fig. 3a and b). The scintillation occurrence maps of $\sigma_\Phi > 0.1$ rad (Fig. 3b) and sDPR $> 2\,mm\,s^{-1}$ (Fig. 3c) show high occurrence in the cusp and in the auroral oval that expanded well beyond its statistical representation. At auroral and subauroral latitudes, scintillation was approximately collocated with radar backscatter from convecting ionospheric irregularities (Fig. 3d), as already discussed above.

Figure 5a shows the sDPR index and ground magnetic field X-component perturbation at Churchill, and riometer absorption observed in Gillam on March 7. With moderately southward IMF B_z prior to the IP shock arrival, the auroral activity at GILL started at 02:30 UT but significantly intensified after the shock arrival at 03:30 UT. The sDPR index is correlated with the ground magnetic field perturbations in Churchill and the riometer absorption increases in Gillam.

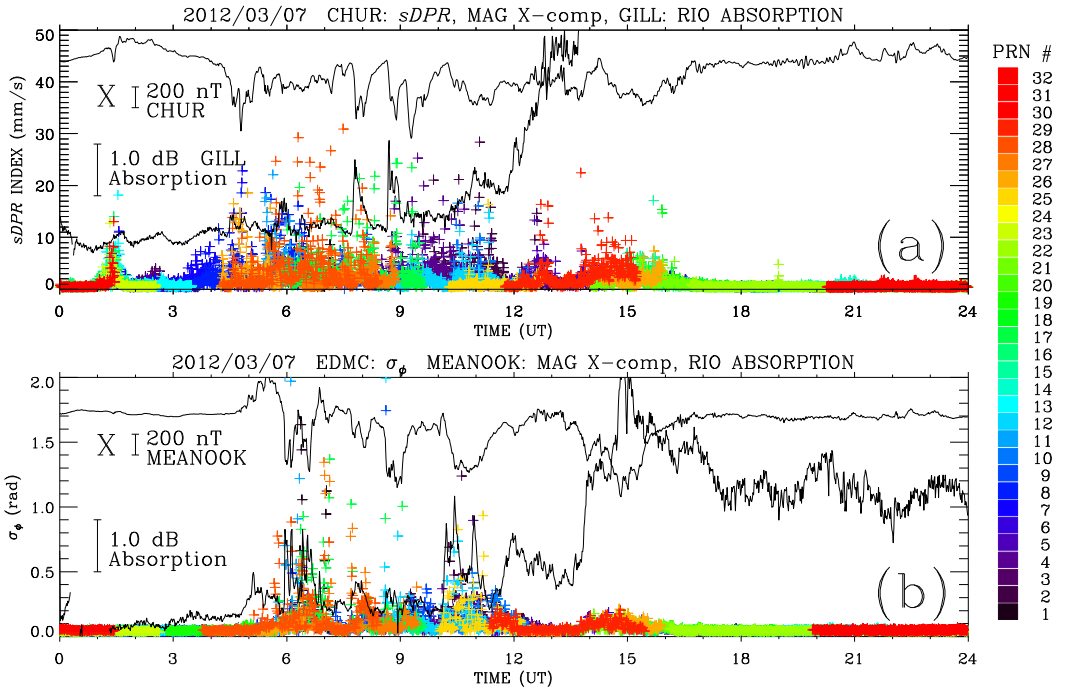

Figure 5. (a) The phase scintillation proxy index sDPR (colored crosses) for elevations above 30°, the X component of the ground magnetic field in Churchill, and the riometer absorption observed in Gillam on 7 March. **(b)** The phase scintillation σ_Φ from a GPS receiver near Edmonton, the X component of the ground magnetic field, and the riometer absorption observed in Meanook on 7 March.

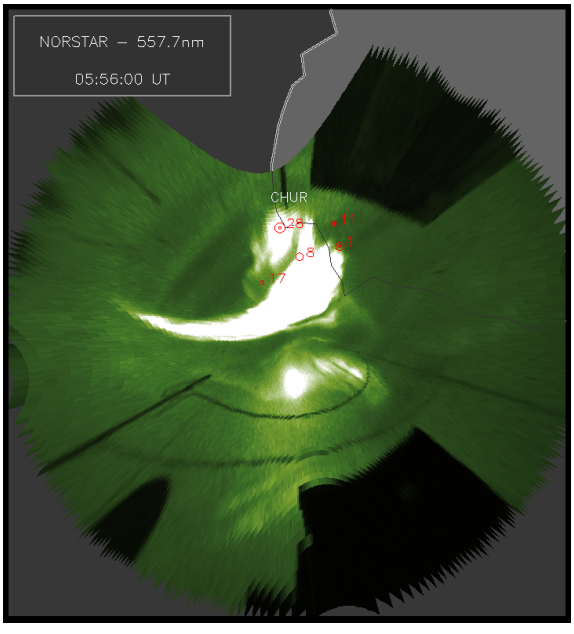

Figure 6. The mapped 557.7 nm auroral emission observed in Gillam at 05:56 UT on 7 March. The IPPs of five GPS satellites for the receiver in Churchill are shown as circles that are scaled proportionally to the 30 s sDPR values between 2 and 10 mm s^{-1}.

The cosmic noise absorption (in dB) observed by riometers at 30 MHz is usually a good proxy for precipitating energetic electron fluxes resulting in auroral emission, but a major polar cap absorption (PCA) caused by energetic protons started at about 12:00 UT, exceeding 6 dB for many hours (off scale in Fig. 5a). At lower auroral latitudes near Edmonton the auroral activity started at ∼ 05:00 UT (Fig. 5b). The phase scintillation σ_Φ observed by the EDMC receiver in Ministik Lake was correlated with the ground magnetic perturbations and riometer absorption in Meanook. Strong scintillation with sDPR exceeding 20 mm s^{-1} was also observed further westward in Whitehorse (WHIT) and Fairbanks (FAIR) as well as eastward in Saskatoon (SASK), Pickle Lake (PICL), and Schefferville (SCH2).

The L-shell-aligned scintillation region expanded equatorward to ∼ 55° of AACGM latitude (Fig. 3c). The IGS receivers observed moderate scintillation across the continent, from Calgary (PRDS) and Winnipeg (WINN) to Val d'Or (VALD) around 58° of AACGM latitude from 06:00 to 12:00 UT. Weak scintillation (sDPR ≈ 2 mm s^{-1}) was observed down to ∼ 54° of AACGM latitude, from Chilliwack (CHWK) to Ottawa (NRC1) and Fredericton (FRDR), near the equatorward border of scintillation region at the poleward edge of the main trough (shown below).

Several NORSTAR ASIs observed aurora after ∼ 04:00 UT. Figure 6 shows an example of the mapped ASI image with the scintillation IPPs for the CHUR receiver

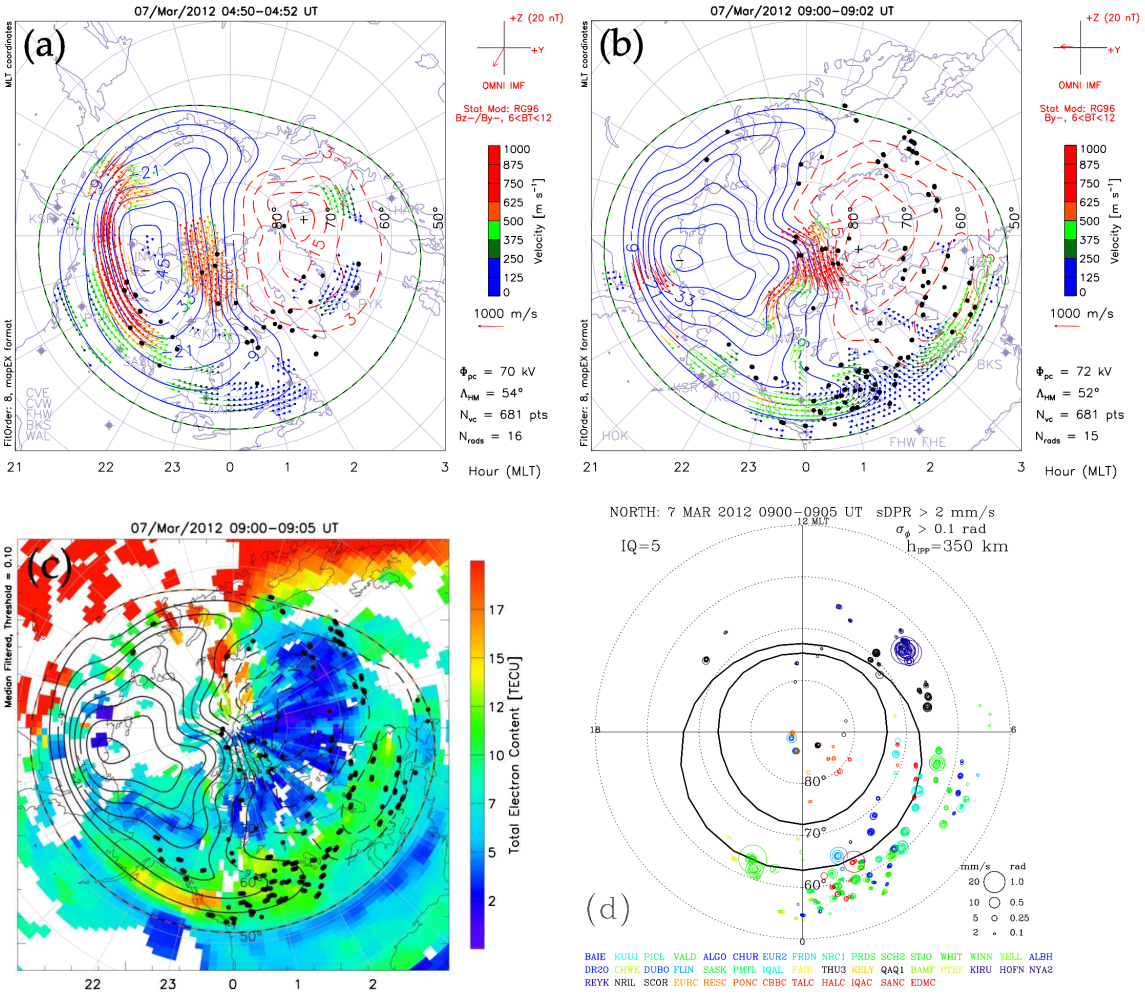

Figure 7. (a–b) Event S1: SuperDARN convection and potential maps on 7 March. The IPPs for PRNs with $\sigma_\Phi > 0.1$ rad or sDPR > 2 mm s^{-1} are superposed as black dots. **(c)** The 5 min median-filtered TEC mapped in coordinates of AACGM latitude and MLT is overlaid with the SuperDARN potential map and IPPs (black dots) for $\sigma_\Phi > 0.1$ rad or sDPR > 2 mm s^{-1} on 7 March between 09:00 and 09:05 UT. **(d)** The IPPs are shown as circles scaled proportionally to σ_Φ and sDPR values.

superposed. The mapping on a geographic grid assumes a height of 110 km for both the 557.7 nm auroral emission and IPPs. The scintillation (sDPR > 2 mm s^{-1}) was collocated with a spiral auroral form as it brightened.

The SuperDARN convection map at 04:50 UT (Fig. 7a) shows very high ionospheric velocities exceeding 1 km s^{-1} in the dusk sector and the central polar cap, a result of large southward IMF and a sudden impulse (SI) at ∼ 04:20 UT. The 350 km IPPs with scintillation index $\sigma_\Phi > 0.1$ rad and sDPR > 2 mm s^{-1} between 04:50 and 04:52 UT were collocated with the strong convection in the dusk convection cell and in the central polar cap but also mapped to the convection exit region, where there was no backscatter observed at this time but where the antisunward convection would transport polar cap patches turning into auroral blobs, which are known to cause strong scintillation (Jin et al., 2014). The convection zone as marked by the Heppner–Maynard (H-M) boundary (Imber et al., 2013) moved from ∼ 60 to 50° of magnetic latitude (Fig. 7b). The scintillation IPPs map to a strong antisunward convection in the central polar cap and to the expanded convection in the exit region turning duskward and dawnward. There is a possibility of SAPSs at the equatorward edge of the return flow just poleward of the main trough as it was in the case reported by Makarevich and Bristow (2014). During the same event, the SAPS was collocated with a weak scintillation (sDPR < 5 mm s^{-1}) (Prikryl et al., 2015b) (further discussed below).

Figure 7c shows a 5 min mean TEC map overlaid with the electrostatic potential contours and scintillation IPPs. Using the same coordinate system of AACGM latitude and MLT, Fig. 7d shows the IPPs as circles that are sized proportionally to σ_Φ and sDPR values as shown in the bottom right corner. We refer to these threshold values approximately defining weak ($\sigma_\Phi < 0.25$ rad; sDPR < 5 mm s^{-1}),

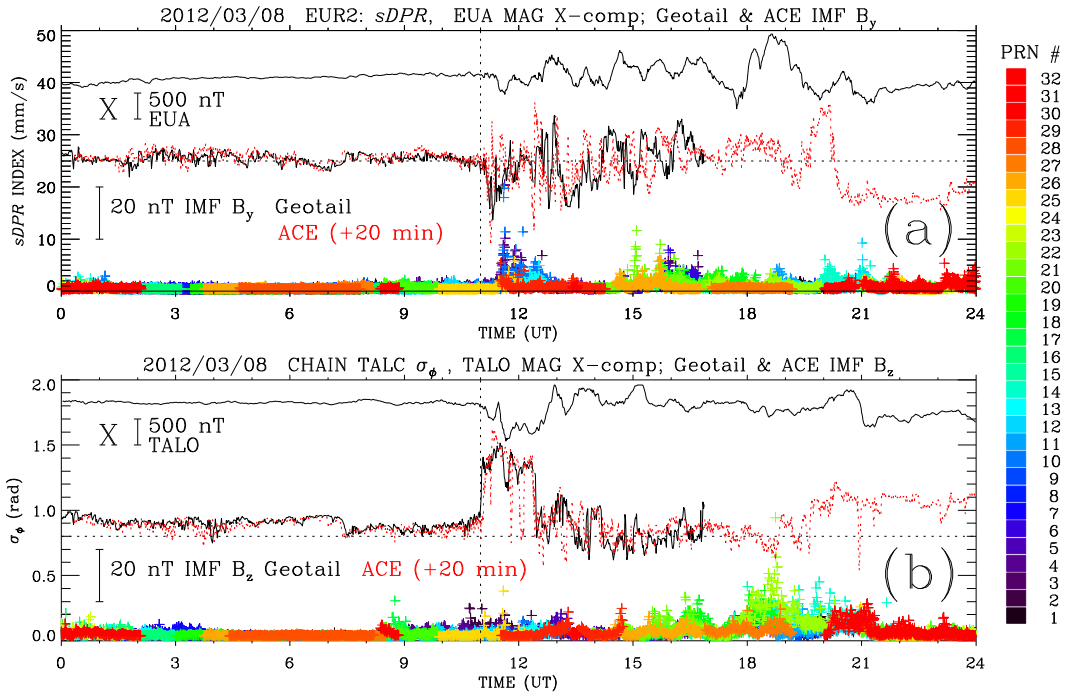

Figure 8. (a) The phase scintillation proxy index sDPR (colored crosses) for elevations above 30°, and the X component of the ground magnetic field at Eureka. **(b)** The phase scintillation σ_Φ, the X component of the ground magnetic field observed in Taloyoak, and the IMF B_z. The dotted vertical line indicates the interplanetary shock arrival time at Geotail. Superposed in **(a)** and **(b)** is the IMF B_y in geocentric solar ecliptic (GSE) coordinates observed by Geotail before it entered the post-noon magnetosheath and ACE in the upstream solar wind (dotted red line; shifted by 20 min).

moderate ($0.25 < \sigma_\Phi < 0.5$ rad; $5 < \text{sDPR} < 10$ mm s^{-1}), and strong ($\sigma_\Phi > 0.5$ rad; sDPR > 10 mm s^{-1}) scintillation. A statistical auroral oval is shown for IQ = 5. On the dayside, a few weak scintillation IPPs map to TOI and a patch detached from it. In the central polar cap, weak to moderate scintillation IPPs map to moderately enhanced TEC due to patches convecting antisunward. A burst of strong scintillation was observed at the edge of high-latitude trough poleward of enhanced TEC over Iceland (HOFN and REYK) in the morning sector and northwestern Canada (WHIT) in the pre-midnight sector. A dense cluster of IPPs of moderate to strong scintillation was collocated with enhanced TEC in the nightside auroral oval and weak scintillation mapped to the poleward edge of the main trough, particularly near midnight, where SAPSs may have been present (Prikryl et al., 2015a).

5 Event S2: 8–9 March 2012 – case of IMF $B_z > 0$ reversing to IMF $B_z < 0$

The second ICME shock (Fig. 2) occurred on 8 March during a steady but moderate northward IMF B_z that subsequently increased to large values exceeding +30 nT observed by ACE and Geotail (Fig. 10b). The shock magnetosonic Mach number was 9.4, causing a significant SI (see T8, their Table 2), and SYM-H reached +54 nT at 11:06 UT (Fig. 2g). The northward IMF conditions are conducive to transpolar arcs that were observed drifting over Resolute Bay until the ASI was shut off at 10:30 UT. Faint transpolar arcs were also observed by SSUSI during a DMSP F18 satellite pass centered at ∼ 10:19 UT (not shown). There was only weak scintillation observed in the polar cap at this time (RESC and THU3). At 11:30 UT, scintillation suddenly peaked, with σ_Φ reaching up to 1.5 rad as observed at EURC (not shown), and sDPR peaked at ∼ 20 mm s^{-1} at EUR2 for satellite 10 (Fig. 8a). The IMF measured by ACE and Geotail (Fig. 8a and b) showed a jump in B_z of ∼ 20 nT at the IP shock followed by large-amplitude oscillations of B_y. The ACE time series are shifted by 20 min to match the shock observed by Geotail (Kokubun et al., 1994), which was located in front of the Earth's bow several hours before entering the magnetosheath. The strong scintillation onset at EURC (and THU3) occurred just after the IMF B_y oscillated between duskward and dawnward (Fig. 8a), while B_z remained strongly northward (Fig. 8b). Weak to moderate scintillation continued in the polar cap for the rest of the day, while the ground magnetic field in Eureka remained perturbed by the IMF fluctuations. There were no ASI data, but particle precipitation into transpolar arcs was observed during northern and southern high-latitude overpasses by DMSP satellites. While passing over the northern polar cap, the DMSP F18 particle detec-

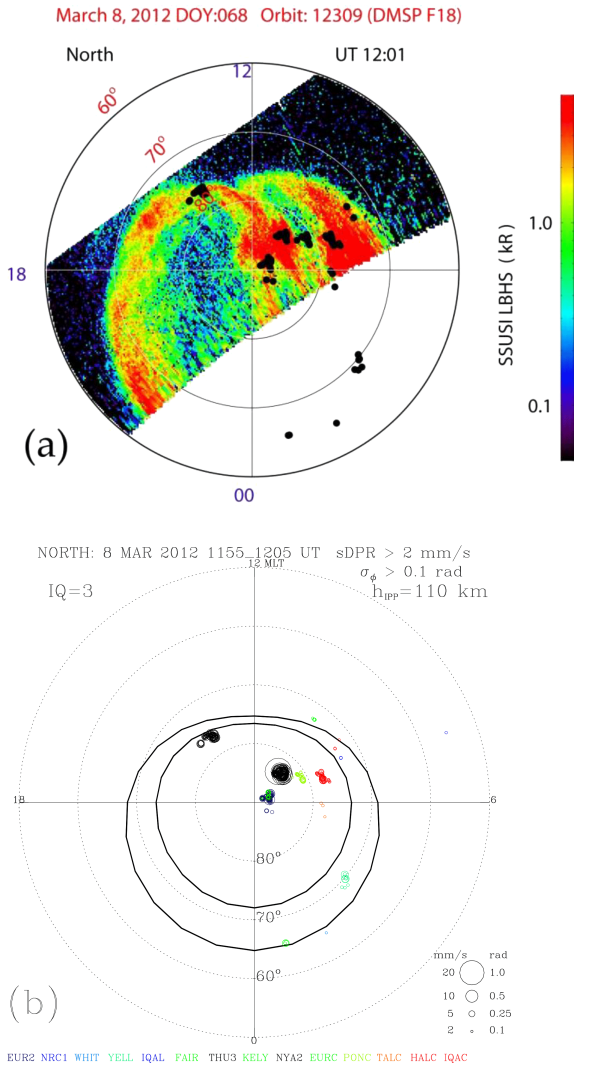

Figure 9. (a) SSUSI (DMSP F18) auroral image scans mapped as a function of AACGM latitude and MLT. Superposed (black dots) are IPPs where scintillation $\sigma_\Phi > 0.1$ rad or sDPR > 2 mm s^{-1}. **(b)** The IPPs are shown as circles scaled proportionally to σ_Φ and sDPR values.

tors observed electron precipitation fluxes with energies of ∼ 3 keV (http://sd-www.jhuapl.edu/Aurora/), indicating the presence of auroral arcs (Newell et al., 2009). The SSUSI image scan (Fig. 9a) observed intense transpolar arcs. Superposed on the image are scintillation IPPs at 110 km during an F18 pass between 11:55 and 12:05 UT indicating moderate to strong scintillation in Eureka and Thule (Fig. 9b) collocated with a transpolar arc and weaker scintillation in the auroral oval. Several hours later, moderate to strong scintillation was observed in the cusp (PONC, HALC, CBBC, and TALC; Fig. 8b), but no scintillation was observed at low auroral latitudes (e.g., EDMC; Fig. 2), which is consistent with mostly northward IMF throughout the day.

On 9 March, after ∼ 02:00 UT, when the IMF B_z reversed to strongly southward (−18 nT), the AE index exceeded 2000 nT and the SYM-H index dipped to −148 nT, resulting in the strongest geomagnetic storm of the interval under study. Strong phase scintillation was observed in the nightside, primarily post-midnight, auroral oval (Fig. 3b and c). Similar to event S1, the scintillation band expanded well beyond the statistical oval and was approximately collocated with the radar backscatter from irregularities moving at a line-of-sight velocity of $V_{LOS} > 100$ m s^{-1} (Fig. 3d).

Figure 10a and b show σ_Φ and sDPR scintillation indices for CHUR and EDMC, respectively. The ground magnetic field X-component perturbation at Churchill and Meanook, as well as riometer absorption observed in Gillam and Meanook, is superposed. In general, scintillation coincided with periods of the ground magnetic perturbations and riometer absorption increases. It should be noted that a one-to-one correlation between scintillation and riometer absorption or magnetic perturbations is not expected because the riometer dipole antenna has a broad 3 dB beam width of ∼ 60° and ground magnetometers respond to ionospheric currents over a large area.

The ASI in Gillam observed auroral breakups starting from ∼ 02:00 UT. Figure 11 shows two auroral images mapped on a geographic grid with IPPs superposed as circles scaled proportionally to sDPR values exceeding 2 mm s^{-1}. CHUR receiver observed a burst of scintillation that was collocated with a rayed auroral arc moving southward from Churchill. At ∼ 06:20 UT, a substorm onset over Gillam triggered intense scintillation observed in Churchill (Fig. 10a). It is noted that this substorm was preceded by an intensification of antisunward flows in the central polar cap, with the polar cap cross-potential increasing from 54 kV at 05:54 UT to 83 kV at 06:14 UT (Fig. 12a). At this time the return flows also increased near the local midnight (Fig. 12a) and later intensified in the dawn sector (Fig. 12b). Phase scintillation was observed in the polar cap and in the auroral oval, where it was collocated with return convection (Fig. 12a and b). This was taking place under conditions of strongly southward IMF B_z and duskward B_y ($B_y > 0$), causing the expanding convection pattern to be tilted relative to magnetic noon–midnight meridian. The antisunward flow carrying polar cap patches toward the pre-midnight auroral oval likely played a role in triggering the substorm. This is consistent with recently discovered relationships between polar cap patches and substorms (Nishimura et al., 2013) and between enhanced polar cap flows and poleward boundary intensifications (Zou at al., 2014).

Figure 12c shows the TEC map overlaid with the electrostatic potential contours and scintillation IPPs. Figure 12d shows the IPPs as circles scaled proportionally to σ_Φ and sDPR values. Most of the IPPs of moderate to very strong scintillation fall within a band of enhanced TEC between 21:00 and 06:00 MLT poleward of the main trough in the nightside auroral oval that expanded well beyond the statisti-

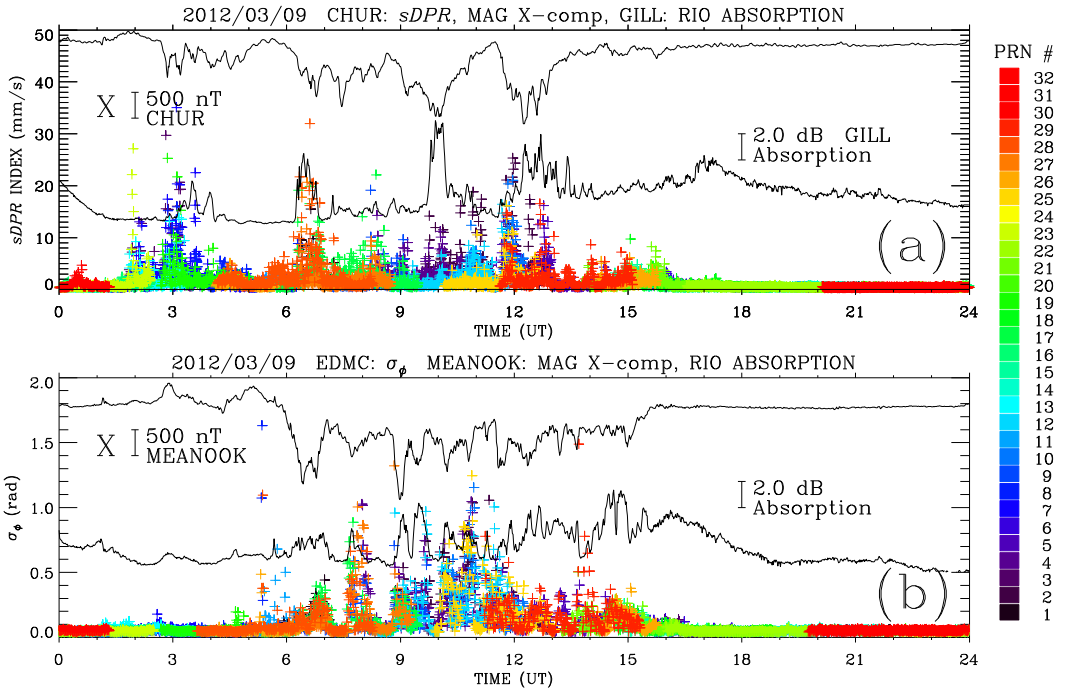

Figure 10. Same as in Fig. 5a and b but for 9 March.

cal oval shown in Fig. 12d. In the noon sector, weak to moderate scintillation was collocated with a fractured TOI that extended from Scandinavia into the polar cap. Some IPPs of weak to moderate scintillation also map to the equatorward border of the dusk and dawn convection cells in regions covered by GPS receivers NRIL in Siberia and REYK in Iceland, respectively.

6 Event S3: 11–12 March 2012 – cases of IMF $B_z \approx 0$ and a strong dynamic pressure pulse

During this "double-shock" event (T8) the ionospheric responses to the first and second shock were quite different. The first IP shock on 11 March was observed by ACE at ∼ 12:59 UT. Geotail, which was near the Earth's bow shock on the dawnside, observed the IP shock at 13:05 UT. It was followed by moderately enhanced proton density and small-amplitude fluctuations in magnetic field, with IMF B_z periodically dipping to small negative values. Because of small and predominantly northward B_z, the convection zone was constrained to above 70° AACGM latitudes for the first few hours after the first shock arrival. At these latitudes, weak to moderate scintillation continued for several hours after the IP shock (Figs. 2f and 3a). Figure 13a shows a narrow dawn cell of tightly wound sunward to antisunward flow with low-level scintillation IPPs collocated primarily with the enhanced convection on the dayside (Fig. 13b). There was very low or no scintillation occurrence in the nightside auroral oval on this day (Figs. 2 and 3).

In contrast, on 12 March, the second IP shock that was observed at ∼ 08:40 UT by ACE and at 09:11 UT by Geotail coincided with very high proton density, velocity, and magnetic field magnitude jumps followed by large-amplitude oscillations of magnetic field components, particularly B_z dipping to −26 nT. The AE index peaked above 1500 nT and the pressure-corrected SYM-H index dipped to −75 nT (T8). The shock that triggered a "supersubstorm" (T8) was promptly followed by an onset of auroral activity, including scintillation (Figs. 2 and 4a). The combination of a strong southward IMF B_z and dynamic pressure pulse resulted in an expanded convection zone with the H-M boundary moving to 50° of magnetic latitude (Fig. 13c). Scintillation occurred at all latitudes, but it was strongest in the expanded auroral oval on the nightside. There was only weak scintillation in the polar cap, where enhanced convection flow was observed, but moderate to strong scintillation mapped to the cusp (NYA2) and the nightside auroral oval from Alaska (FAIR and GAKO) to central Canada (CHUR) (Fig. 13d).

7 Event S4: 15–17 March 2012 – case of a fluctuating IMF producing polar cap patches

This interplanetary event was a combination of an ICME with magnetic cloud (MC) characteristics and an HSS. The AE index exceeded 1500 nT and the SYM-H index dipped to −79 nT on 15 March. The shock was followed by large-amplitude magnetohydrodynamic (MHD) waves with periods of 20–30 min. Figure 14b shows the IMF B_y measured

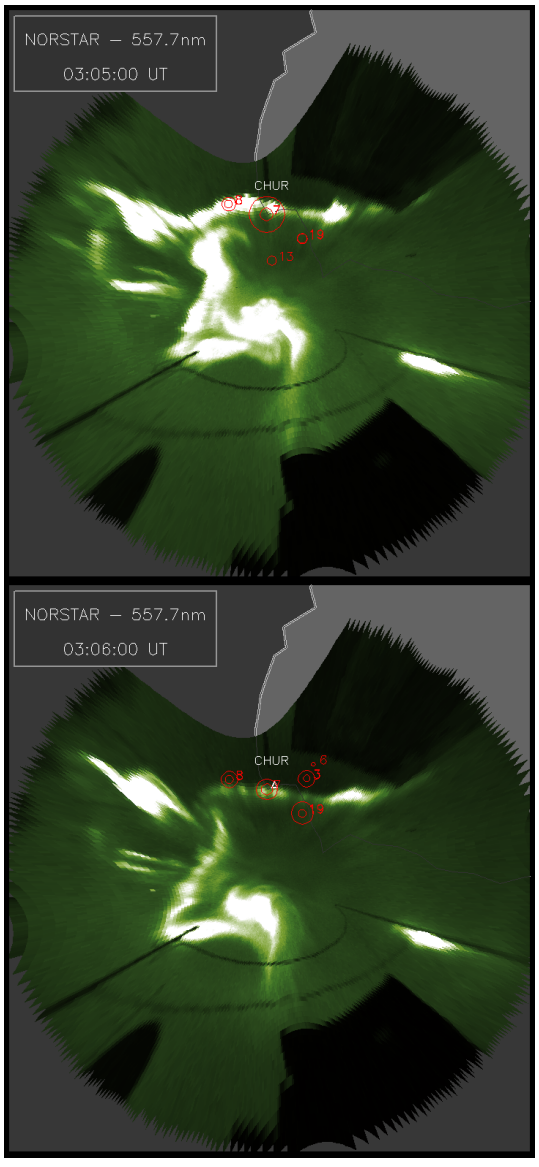

Figure 11. The mapped 557.7 nm auroral emission observed in Gillam at 03:05 and 03:06 UT on 9 March. The IPPs of five GPS satellites for the receiver in Churchill are shown as circles scaled proportionally to the 30 s sDPR values between 2 and 35 mm s^{-1}.

by Geotail after it crossed the dawnside bow shock exiting from the magnetosheath into the solar wind. The IP shock as observed by Geotail is shown by a vertical dotted line. The IMF B_y measured by ACE and shifted by 35 min correlates well with large-amplitude oscillations observed by Geotail. The ground magnetometers and riometers in Rankin and Taloyak observed ULF waves that were accompanied by phase scintillation in Baker Lake (BAKE) and TALO (Fig. 14a and b). During predominantly southward but oscillating IMF the solar wind MHD waves modulated ionospheric convection on the dayside. Pulsed ionospheric flows (PIFs) were observed by Rankin Inlet radar between 12:00 and 17:00 UT (not shown). Figure 15a shows intense flows in the dawn and dusk convection cells on the dayside. The scintillation IPPs occurred primarily with the enhanced convection, but some IPPs also mapped to the polar cap, where the scintillation was caused by convecting polar patches.

After 16:00 UT on 15 March, ACE entered the magnetic cloud characterized by a steady rotating magnetic field. As the IMF B_y rotated from duskward ($B_y > 0$) to dawnward ($B_y < 0$) (Fig. 14b), a TOI scintillation band tilted duskward on 15 March and dawnward on 16 March (Fig. 4b). Figure 15b shows convection and potential maps for IMF $B_y < 0$. The IPPs of enhanced σ_Φ and/or sDPR map to intense convection drawing dense SED plasma into a TOI through the cusp, where it was segmented into patches convected in the polar cap (Fig. 15c). Moderate to strong scintillation was collocated with TOI fragmented into patches and maps to the poleward edge of SED plasma (Fig. 15c and d).

On 16 March, starting from ∼ 08:00 UT and continuing through 17 March, the influence of an HSS that is characterized by solar wind Alfvén waves become dominant. Figure 16a shows the IMF B_y measured by Geotail located just in front of the bow shock in the pre-noon sector. It was correlated with the IMF B_y measured by ACE shifted by 40 min. The variability in IMF B_y is known to result in the production of polar cap patches (Zhang et al., 2011). The patches caused relatively weak but persistent phase scintillation at RESC and EURC. Figure 16a indicates a tendency for stronger scintillation to occur when the ionospheric horizontal drift velocity measured by CADI in Resolute Bay was higher.

8 Discussion

A variety of solar phenomena, including solar flares, coronal mass ejections, and coronal holes, directly or indirectly impacted the Earth's high-latitude ionosphere on 7–17 March 2012. Several X- and M-class flares are listed by Tsurutani et al. (2013, their Table 1). Tsurutani et al. (2005) found a significant response of the dayside ionosphere to high X-ray and EUV fluxes by an abrupt increase in TEC. Riometer absorption due to the ionization produced by a flare can be observed if not masked by often stronger solar radio emissions. However, most of the X-class flares in this interval occurred in dark hours for the North American sector. The X5.4-class flare on 7 March started at 00:17 UT, which is late evening in western Canada. The riometer in Meanook observed some of the initial increase in the cosmic noise absorption caused by the ionization due to this flare, but the absorption was quickly reversed by strong solar radio emission, which presents noise for riometer measurements. The flare-induced ionization does not produce any significant horizontal density gradients or other ionospheric structure that would result in scintillation. Similarly, energetic proton fluxes that caused extensive PCA events observed by riometers (see, for example, Fig. 5) were not associated with GPS scintillation.

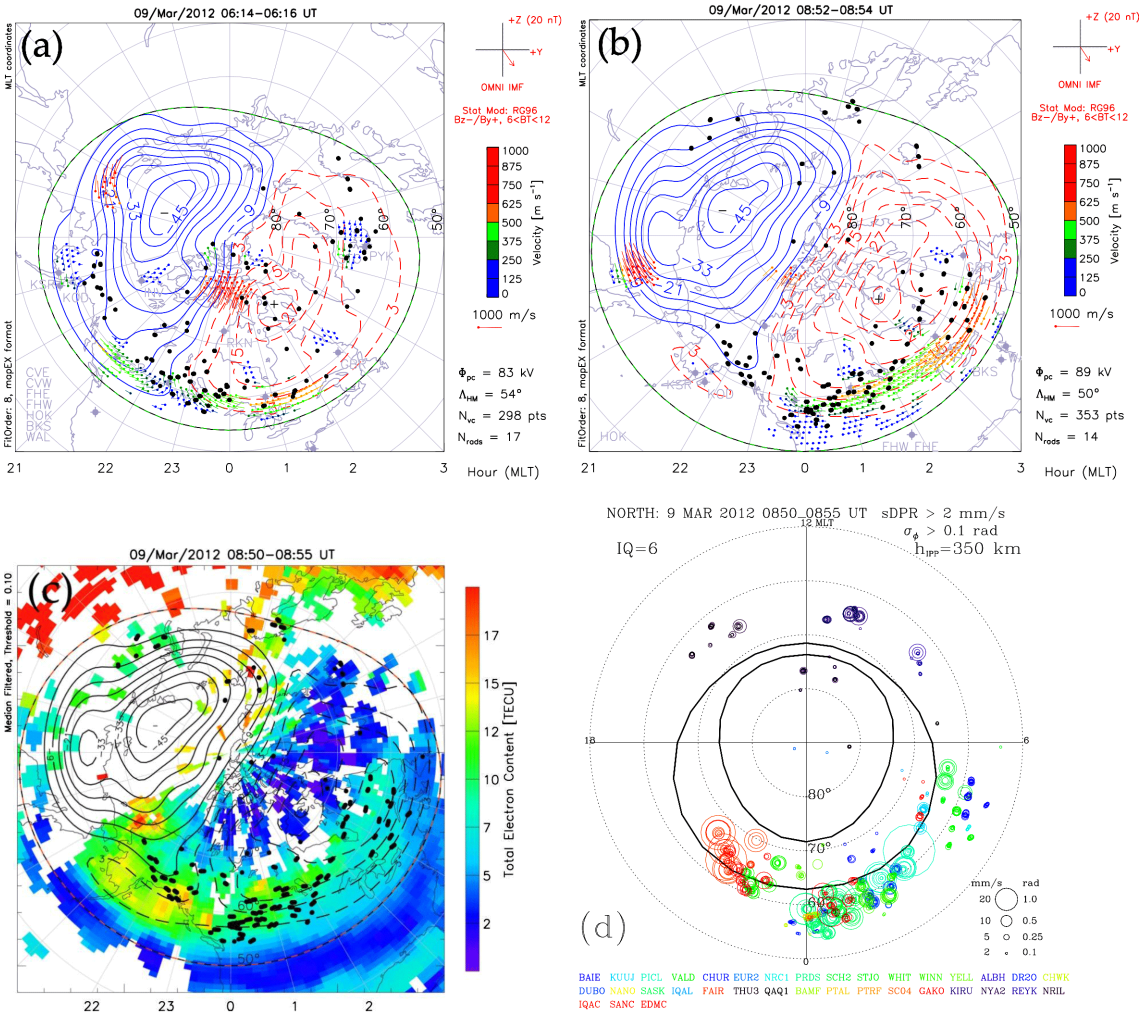

Figure 12. (a, b) Event S2: SuperDARN convection and potential maps on 9 March. The IPPs for PRNs with $\sigma_\Phi > 0.1$ rad or sDPR > 2 mm s^{-1} are superposed as black dots. **(c)** The 5 min median-filtered TEC mapped in coordinates of AACGM latitude and MLT is overlaid with the SuperDARN potential map and IPPs (black dots) for $\sigma_\Phi > 0.1$ rad or sDPR > 2 mm s^{-1}. **(d)** The IPPs are shown as circles scaled proportionally to σ_Φ and sDPR values.

Rather, the high-latitude scintillation of transionospheric radio signals including GNSS is a consequence of solar wind coupling to the magnetosphere that leads to discrete energetic particle injections resulting in sharp electron density gradients and dynamic ionospheric convection of irregularities.

The coupling between variable solar wind and the magnetosphere–ionosphere system strongly affects the structure of the polar, auroral, and subauroral ionosphere that results in scintillation. The ionospheric signatures of the coupling were manifested by the dynamics of ionospheric convection that were observed by SuperDARN (Figs. 7, 12, 13 and 15). They included intense, sometimes pulsed, flows in the cusp, which are the ionospheric signatures of magnetic reconnection between the southward IMF and the northward Earth magnetic field at the dayside magnetopause. These ionospheric flows can have a large extent in longitude and lead to an overall intensification of the dayside convection in the dawn or dusk cells, depending on the IMF B_y polarity that controls the dawn–dusk asymmetry of the ionospheric convection pattern (Ruohoniemi and Greenwald, 2005; Grocott et al., 2010). This is further addressed in the companion paper (Prikryl et al., 2015a).

On the nightside, substorm activity is a consequence of magnetic reconnection in the magnetotail resulting in acceleration of charged particles and aurora that consequently lead to steep density gradients and irregularities causing scintillation. Cases of scintillation coincident with aurora and/or riometer absorption during storms S1 and S2 have been observed (Figs. 5, 6, 10a and b, and 11). However, another consequence of tail reconnection is that newly reconnected magnetic flux is transferred from the magnetotail sunward over the flanks of the magnetosphere. The ionospheric sig-

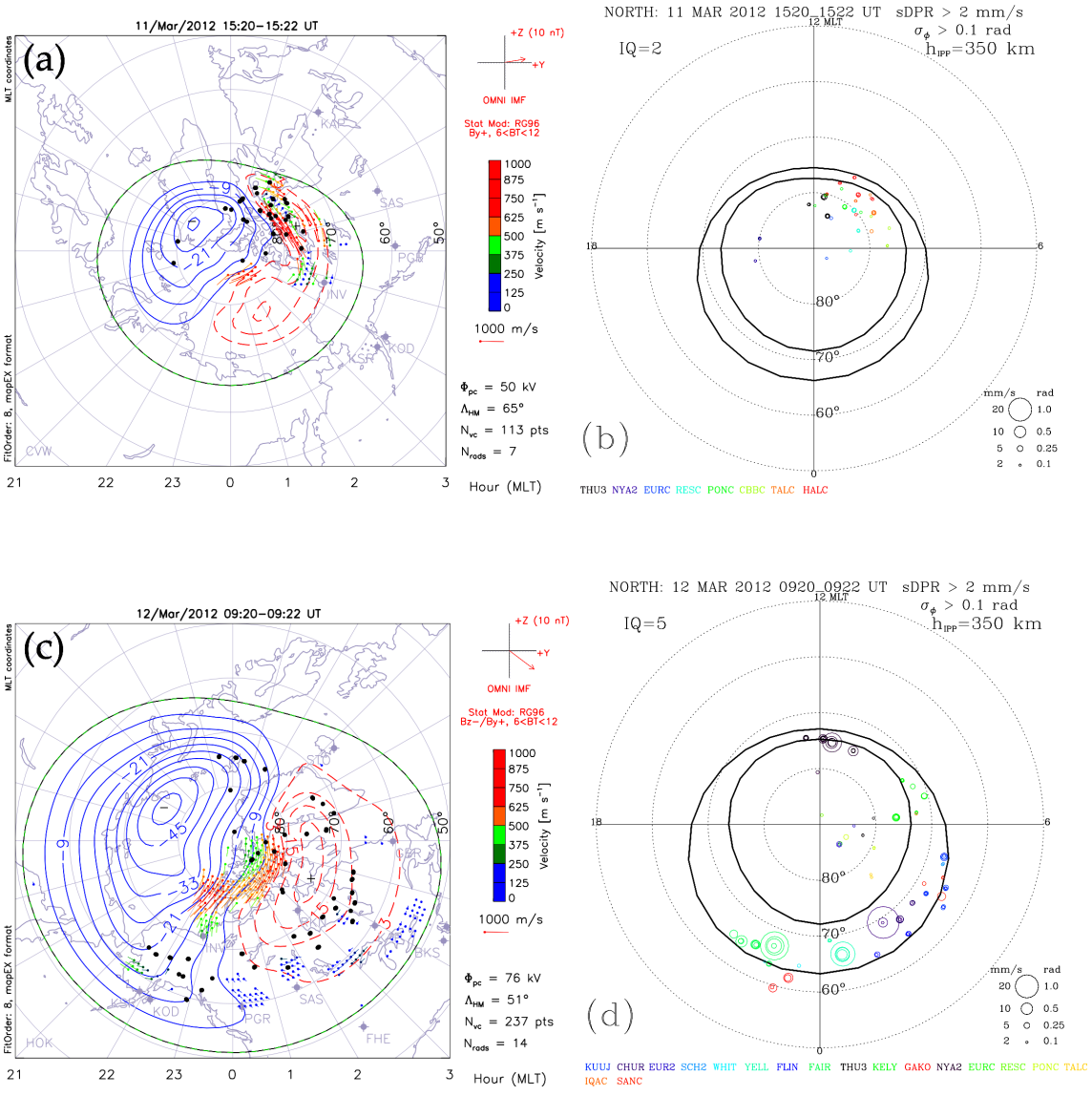

Figure 13. (a, c) Event S3: SuperDARN convection and potential maps on 11 and 12 March. The IPPs for PRNs with $\sigma_\Phi > 0.1$ rad or sDPR > 2 mm s^{-1} are superposed as black dots. **(b, d)** The IPPs are shown as circles that are scaled proportionally to σ_Φ and sDPR values.

nature of this process is the return convection in the ionosphere driven by the magnetospheric electric field mapped along magnetic field lines. Ionospheric irregularities convecting at high speed may cause scintillation with strong return convection present in the dusk (Fig. 7a) or the morning (Figs. 7b, 12b) sectors. The L-shell-aligned scintillation region shifted equatorward following the expansion of convection and H-M boundary.

The ICMEs on 7 and 8–9 March (storms S1 and S2) resulted in the strongest phase scintillation. For the case of IMF $B_z < 0$ (S1 and the second half of S2), the scintillation was linked to bright discrete auroras and riometer absorption due to energetic particle precipitation depositing most of its energy at low altitude, producing ionization in the E and D region. The scintillation IPPs were coincident with bright auroral forms that were mapped assuming an altitude of 110 km. Also, the scintillation IPPs mapped to strong antisunward flows in the central polar cap and to the return convection in the expanded dusk and dawn convection cells.

For the case of strong southward IMF there is a possibility of SAPSs. SAPSs can feature a narrow region of intense flow called a subauroral ion drift (SAID) that is collocated with a TEC enhancement poleward of the TEC trough. Such a case was studied in detail by Makarevich and Bristow (2014, their Fig. 2). SuperDARN observations of SAPSs were previously associated with weak phase scintillation that mapped along the equatorward border of the auroral oval (Prikryl et al., 2013b, 2015b). During storm S1, weak scintillation IPPs

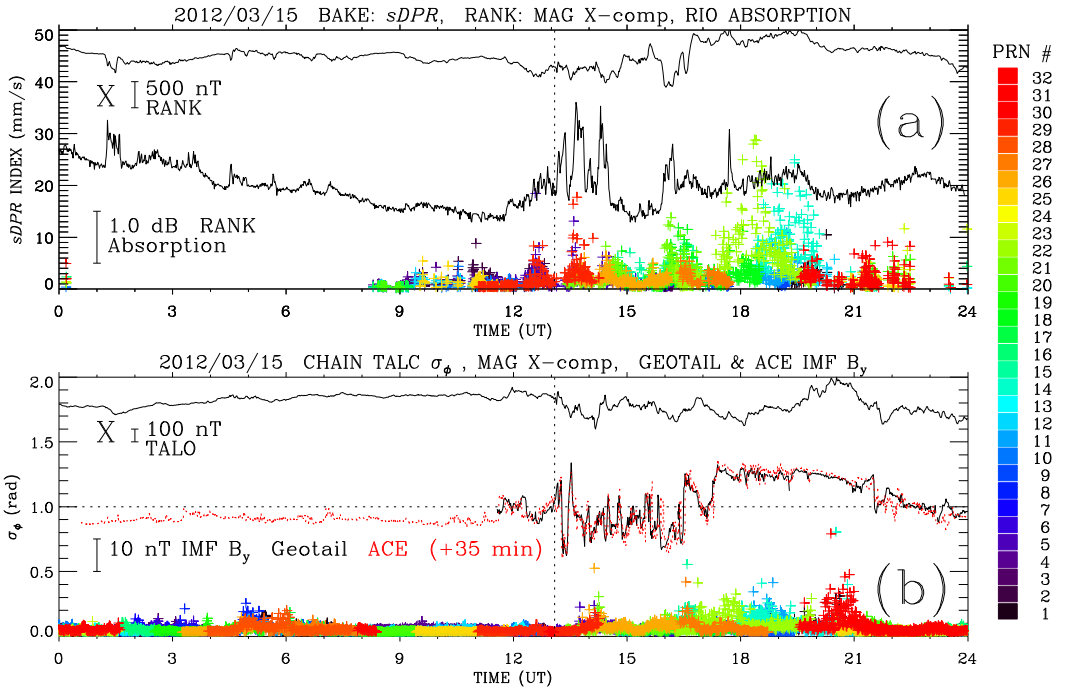

Figure 14. (a) The phase scintillation proxy index sDPR (colored crosses) for elevations above 30° at Baker Lake, the X component of the ground magnetic field, and the riometer absorption observed in Rankin Inlet. **(b)** The phase scintillation σ_Φ from a GPS receiver and the X component of the ground magnetic field observed in Taloyoak. Superposed is the IMF B_y (GSE) observed by Geotail after it crossed the dawnside bow shock exiting from the magnetosheath into the solar wind and ACE (shifted by 35 min) in the upstream solar wind.

scintillation mapped to the poleward edge of the main trough (Fig. 7c), and there is indication of SAPS presence shown in the companion paper (Prikryl et al., 2015a, their Fig. 10a).

In contrast, when the IMF is northward, lobe reconnection can result in dayside sunward flows and multiple convection cell patterns as well as energetic particle precipitation producing transpolar arcs (Cumnock, 2005) that can cause scintillation in the polar cap. The IP shock of event S2 coincided with a large northward IMF component and a strong solar wind dynamic pressure pulse that resulted in bright transpolar arcs causing moderate to strong scintillation (Fig. 9). Scintillation was also observed in the cusp, but no scintillation was observed at low auroral latitudes.

Similar to event S2, the "double-shock" event S3 produced significantly different responses to the first and second shock. The first IP shock that was associated with small IMF resulted in relatively weak scintillation that was confined to high latitudes, with IPPs collocated primarily with the enhanced convection in the dawn cell on the dayside. In contrast, the second IP shock that coincided with a strong solar wind dynamic pressure pulse and southward turning of IMF that triggered a "supersubstorm" lead to an onset of scintillation at all latitudes, but the strongest scintillation was observed in the expanded auroral oval on the nightside (Fig. 13d).

Through coupling to the dayside magnetopause, the solar wind Alfvén waves can generate a series of polar patches that are convected in the central polar cap (Prikryl et al., 1999). The fluctuating IMF during storm event S4, which was a combination of an ICME magnetic cloud and an Alfvénic HSS, produced copious polar cap patches observed by ionosonde (Fig. 16b). Two solar wind monitors, ACE and Geotail, were located approximately on the same Parker spiral, which resulted in good correlation of IMF fluctuations observed by the two spacecraft. Geotail was located near the bow shock on the dawnside, which gives confidence that the observed fluctuations (MHD/Alfvén waves) impacted the subsolar magnetopause driving pulsed reconnection, or directly affected the open field lines in the polar cap. Solar wind MHD waves, Alfvén waves in particular, drive mesoscale convection flows in the cusp and on the open magnetic field lines in the polar cap, leading to formation of polar patches when IMF $B_z < 0$. The scintillation was collocated with intense antisunward convection, and TOI fractured into patches drawn in from the high-density solar-illuminated ionospheric plasma (Fig. 15c). The dawn–dusk component of the IMF controls MLT of TOI plasma entry through the cusp and the orientation of the band of enhanced scintillation occurrence as a function of magnetic latitude and MLT. During storm event S4, on 15 and 16 March (Fig. 4b), the band of scintillation within the TOI emerging from the

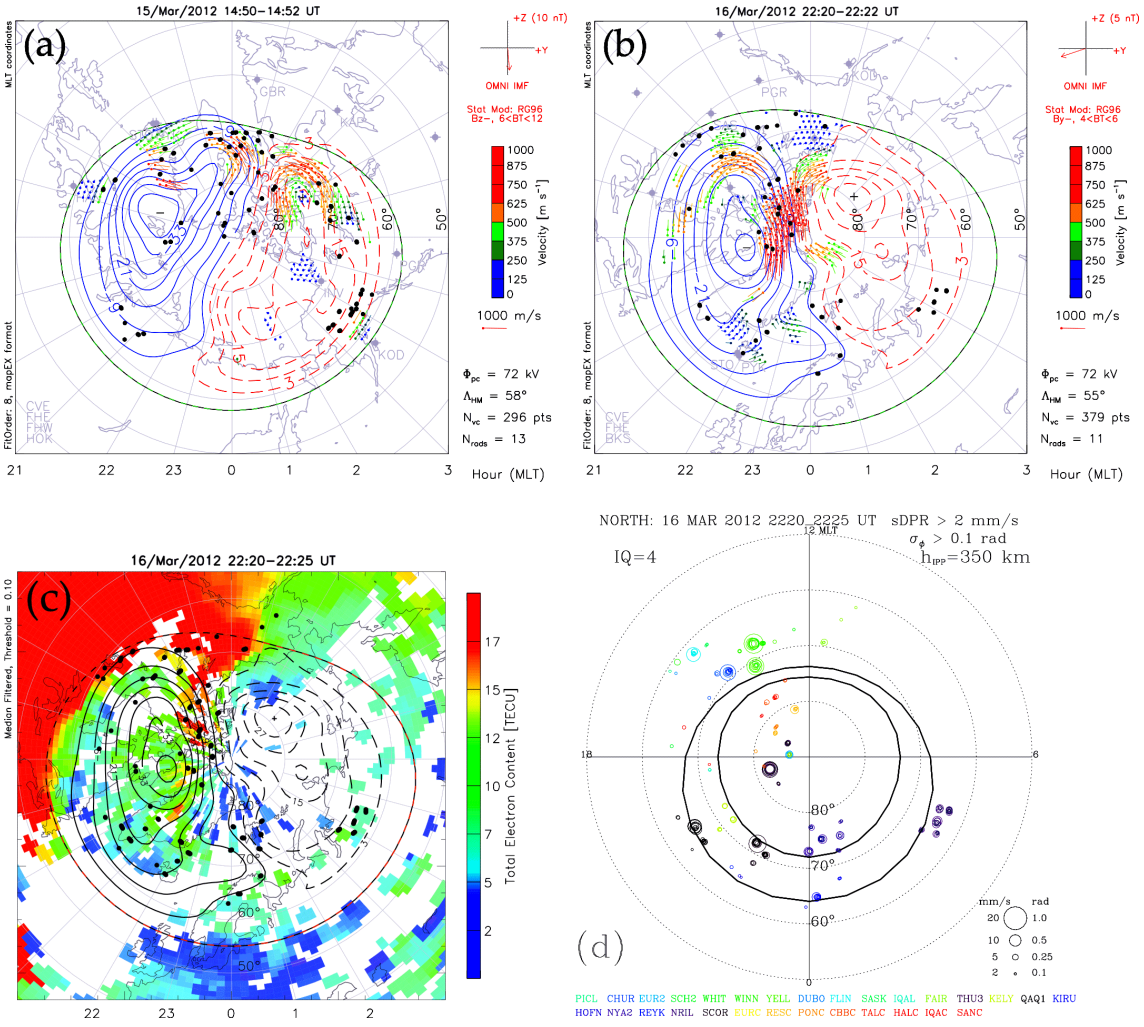

Figure 15. (a–b) Event S4: SuperDARN convection and potential maps on 15 and 16 March. The IPPs for PRNs with $\sigma_\Phi > 0.1$ rad and/or sDPR > 2 mm s^{-1} are superposed as black dots. **(c)** The 5 min median-filtered TEC mapped in coordinates of AACGM latitude and MLT is overlaid with the SuperDARN potential map and IPPs (black dots) for $\sigma_\Phi > 0.1$ rad or DPR > 2 mm s^{-1}. **(d)** The IPPs are shown as circles scaled proportionally to σ_Φ and sDPR values.

cusp was tilted dawnward or duskward for IMF $B_Y > 0$ and $B_Y < 0$, respectively. This is consistent with previous results and has been shown for other storm events (Prikryl et al., 2013b, 2015b). In the central polar cap, the patches caused relatively weak but persistent phase scintillation with a tendency for scintillation to occur when ionosondes measured enhancements in horizontal drift velocity (Fig. 16a).

Anti-sunward flows in the central and nightside polar cap that transport polar cap patches toward the auroral oval were linked to polar boundary intensifications (PBIs) and substorm intensifications. Nishimura et al. (2013) suggested that polar cap patches often precede PBIs and substorm intensifications. Zou et al. (2014) found a statistical relationship between enhanced polar cap flows and PBIs. During storm event S2, an auroral substorm was preceded by strong anti-sunward flows in the central polar cap (Fig. 12a) that were followed by an intensification of nightside convection and an auroral band of scintillation in the midnight sector. This event occurred under conditions of strongly southward IMF B_z and duskward B_y ($B_y > 0$). The convection pattern was tilted with antisunward flow of enhanced density plasma (polar cap patches) directed toward the pre-midnight auroral oval and likely played a role in triggering the substorm.

It is often assumed that TOI is drawn from the high-density solar-illuminated plasma in the dayside ionosphere. However, during storms TOI is drawn from SED plumes of ionization at subauroral latitudes (Foster et al., 2004; Foster and Burke, 2002). These plumes of plasma with a source in the plasmasphere are carried sunward and poleward by the low-latitude edge of SAPSs (Foster et al., 2005) and the convection electric field playing a controlling role in generating TOIs (Thomas et al., 2013). The steep density gradients and

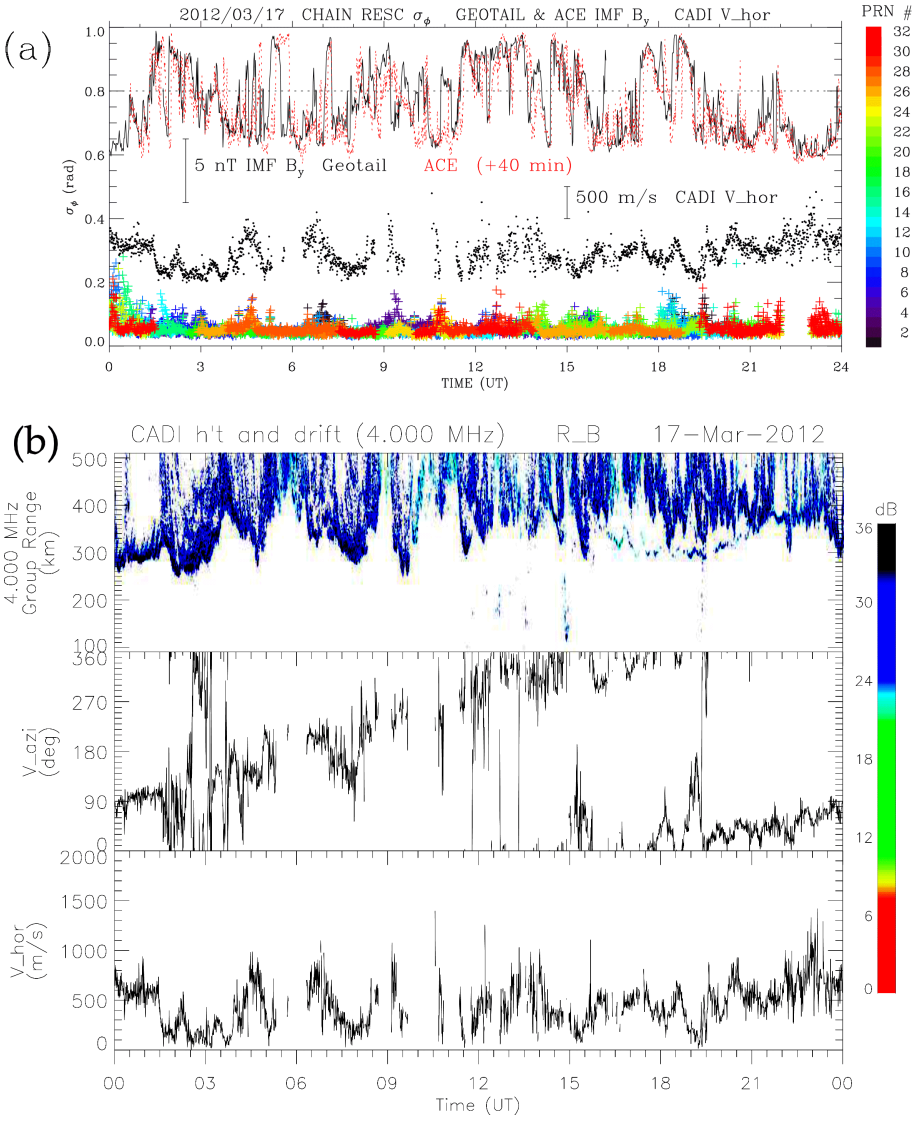

Figure 16. (a) The IMF B_y (GSE) observed by ACE (shifted by 40 min) and Geotail in front of the Earth's bow shock. The RESC CADI horizontal drift velocity is superposed above the plot of phase scintillation index σ_Φ for the GPS receiver RESC at elevations above 30°. **(b)** Fixed frequency ionograms and drift measurements by CADI at Resolute Bay.

irregularities at the poleward edge of an SED plume can result in moderate to strong scintillation as shown in Fig. 15c and d.

9 Summary and conclusions

High-latitude ionospheric responses to variable solar wind during the CAWSES-II interval of study of 7–17 March 2012 were observed in the North American sector. On the ground, they were observed by arrays of GPS receivers, HF radars, ionosondes, riometers, magnetometers, and auroral imagers, and from space they were observed by particle detectors, magnetometers, and a scanning auroral imager on satellites. Primary solar wind drivers of the ionospheric dynamics that resulted in GPS phase scintillation were ICMEs that affected the near geospace and caused weak to moderate geomagnetic storms. Following the overview of interplanetary features by Tsurutani et al. (2014), four geomagnetic storm events, S1 to S4, that were initiated by IP shocks are examined.

Large southward IMF that occurred during night for North America (event S1, second day of S2, and the second shock of event S3) resulted in the strongest auroral response, with auroral breakups and substorms being the main cause of scintillation that was observed at auroral latitudes. As the auroral oval expanded equatorward, moderate to strong scintillation was observed with intense convection in the midnight and early morning sectors. Weak scintillation that was detected at subauroral latitudes near the poleward edge of the main iono-

spheric trough may be attributed to a subauroral polarization stream. In the polar cap, enhanced scintillation mapped to strong antisunward flows. In one case (second day of S2), a strong antisunward flow was followed by an intensification of nightside convection and a substorm, resulting in moderate to strong scintillation in the auroral oval midnight sector. The second IP shock of event S3 that coincided with a strong solar wind dynamic pressure pulse and IMF turning southward led to an onset of scintillation at all latitudes, but the strongest scintillation was observed in the expanded auroral oval on the nightside.

The shocks that impacted the magnetosphere in the morning hours for North America were accompanied with a large northward IMF (S2 and S4) or weak but fluctuating IMF (the first shock of S3). The immediate ionospheric response was observed on the dayside, where scintillation mainly affected the cusp and the polar cap. In one case (S2), a large northward IMF that coincided with a strong solar wind dynamic pressure pulse resulted in scintillation in the polar cap that was caused by intense transpolar arcs. In the case of the first shock of event S3, relatively weak scintillation that was confined to high latitudes was collocated with enhanced dayside convection. In the case of event S4, the initially northward IMF reversed to southward and fluctuated. The arrival of ICMEs coincided with a high-speed stream characterized by large-amplitude Alfvén waves driving convection flows in the cusp and in the polar cap. Moderate to strong scintillation mapped to the poleward edge of the dayside storm enhanced density (SED) plasma, where a dense tongue of ionization (TOI) originated. TOI was segmented into a series of patches that were observed in the polar cap by ionosondes. Moderate scintillation was collocated with the dayside convection enhancements in the cusp and with convecting polar cap patches. The orientation of the scintillation occurrence band in the polar cap was consistent with the prevailing polarity of IMF B_y that controls the dawn–dusk asymmetry of the convection pattern and magnetic local time of TOI entry through the cusp.

In conclusion, the multi-instrument observations during geomagnetic storms were used to identify ionospheric regions of enhanced scintillation in the context of coupling processes between solar wind and the magnetosphere–ionosphere system. The ionospheric response varied with the IMF magnitude and orientation as well as solar wind dynamic pressure. In the auroral oval, scintillation was collocated with auroral breakups and substorms. As the auroral oval expanded equatorward, moderate to strong scintillation was observed with intense convection. Weak scintillation that was detected near the poleward edge of the main ionospheric trough in the midnight sector may be attributed to a subauroral polarization stream. In the polar cap, during southward IMF, enhanced scintillation mapped to convecting patches that were detached from TOI drawn through the cusp from SED plasma. After a strong northward turning of IMF coinciding with a pressure pulse, scintillation in the polar cap was caused by intense transpolar arcs.

Acknowledgements. Infrastructure funding for CHAIN was provided by the Canada Foundation for Innovation and the New Brunswick Innovation Foundation. CHAIN and CGSM operation is conducted in collaboration with the Canadian Space Agency (CSA). The magnetometer and riometer operation and data processing was supported by the Geomagnetic Laboratory, Natural Resources Canada. The Virginia Tech authors acknowledge the support of NSF awards AGS-0838219 and AGS-0946900. The authors acknowledge the use of SuperDARN data. SuperDARN is a collection of radars funded by national scientific funding agencies of Australia, Canada, China, France, Japan, South Africa, the United Kingdom, and the United States of America. The DMSP particle detectors were designed by Dave Hardy of the Air Force Research Laboratory, and the data were obtained from Johns Hopkins University Applied Research Laboratory. The International GNSS Service (IGS) and its contributing organizations, including Denmark Technical University National Space Institute, are thanked for 1 Hz GPS data. We acknowledge use of NASA/GSFC's Space Physics Data Facility's OMNIWeb and CDAWeb service as well as OMNI data. We acknowledge contributions of the ACE, Geotail and Wind teams. This work was supported by the Public Safety Geosciences program of the Natural Resources Canada, Earth Sciences Sector (NRCan ESS contribution number 20140371).

The topical editor K. Hosokawa thanks the two anonymous referees for help in evaluating this paper.

References

Aarons, J.: Global positioning system phase fluctuations at auroral latitudes, J. Geophys. Res., 102, 17219–17231, doi:10.1029/97JA01118, 1997.

Aarons, J., Lin, B., Mendillo, M., Liou, K., and Codrescu, M.: Global Positioning System phase fluctuations and ultraviolet images from the Polar satellite, J. Geophys. Res., 105, 5201–5213, doi:10.1029/1999JA900409, 2000.

Andalsvik, Y. L. and Jacobsen, K. S.: Observed high-latitude GNSS disturbances during a less-than-minor geomagnetic storm, Radio Sci., 49, 1277–1288, doi:10.1002/2014RS005418, 2014.

Aquino, M., Dodson, A., Souter, J., and Moore, T.: Ionospheric scintillation effects on GPS carrier phase positioning accuracy at auroral and sub-auroral latitudes, in: Dynamic Planet, International Association of Geodesy Symposia, 130, edited by: Tregoning, P. and Rizos, C., Springer, Berlin, 859–866, doi:10.1007/978-3-540-49350-1_121, 2007.

Baker, K. B. and Wing, S.: A new magnetic coordinate system for conjugate studies at high latitudes, J. Geophys. Res., 94, 9139–9143, 1989.

Basu, S., MacKenzie, E. M., Basu, Su., Costa, E., Fougere, P. F., Carlson, H. C. Jr, and Whitney, H. E.: 250 MHz/GHz scintillation parameters in the equatorial, polar, and auroral environments, IEEE J. Sel. Area. Comm., SAC-2, 102–115, 1987.

Basu, S., Basu, S., Sojka, J. J., Schunk, R. W., and MacKenzie, E.: Macroscale modeling and mesoscale observations of plasma density structures in the polar cap, Geophys. Res. Lett., 22, 881–884, doi:10.1029/95GL00467, 1995.

Basu, S., Weber, E. J., Bullett, T. W., Keskinen, M. J., MacKenzie, E., Doherty, P., Sheehan, R., Kuenzler, H., Ning, P., and Bongiolatti, J.: Characteristics of plasma structuring in the cusp/cleft region at Svalbard, Radio Sci 33, 1885–1899, doi:10.1029/98RS01597, 1998.

Carlson, H. C.: Sharpening our thinking about polar cap ionospheric patch morphology, research, and mitigation techniques, Radio Sci., 47, RS0L21, doi:10.1029/2011RS004946, 2012.

Chisham, G., Lester, M., Milan, S. E., Freeman, M. P., Bristow, W. A., Grocott, A., McWilliams, K. A., Ruohoniemi, J. M., Yeoman, T. K., Dyson, P. L., Greenwald, R. A., Kikuchi, T., Pinnock, M., Rash, J. P. S., Sato, N., Sofko, G. J., Villain J.-P., and Walker, A. D. M.: A decade of the Super Dual Auroral Radar Network (SuperDARN): Scientific achievements, new techniques and future directions, Survey Geophys., 28, 33–109, doi:10.1007/s10712-007-9017-8, 2007.

Clausen, L. B. N., Baker, J. B. H., Ruohoniemi, J. M., Greenwald, R. A., Thomas, E. G., Shepherd, S. G., Talaat, E. R., Bristow, W. A., Zheng, Y., Coster, A. J., and Sazykin, S.: Large-scale observations of a subauroral polarization stream by midlatitude SuperDARN radars: Instantaneous longitudinal velocity variations, J. Geophys. Res., 117, A05306, doi:10.1029/2011JA017232, 2012.

Cumnock, J. A.: High-latitude aurora during steady northward interplanetary magnetic field and changing IMF By, J. Geophys. Res., 110, A02304, doi:10.1029/2004JA010867, 2005.

Donovan, E., Trondsen, T., Cogger, L., and Jackel, B.: Auroral imaging within the Canadian CANOPUS and NORSTAR projects, Sodankylä Geophysical Observatory Publications, 92, 109–112, 2003.

Feldstein, Y. I. and Starkov, G. V.: Dynamics of auroral belt and polar geomagnetic disturbances, Planet. Space Sci., 15, 209–230, 1967.

Foster, J. C.: Storm time plasma transport at middle and high latitudes, J. Geophys. Res., 98, 1675–1689, doi:10.1029/92JA02032, 1993.

Foster, J. C. and Burke, W. J.: SAPS: A new categorization for sub-auroral electric fields, Eos Trans. AGU, 83, 393–394, doi:10.1029/2002EO000289, 2002.

Foster, J. C., Coster, A. J., Erickson, P. J., Rich, F. J., and Sandel, B. R.: Stormtime observations of the flux of plasmaspheric ions to the dayside cusp/magnetopause, Geophys. Res. Lett., 31, L08809, doi:10.1029/2004GL020082, 2004.

Foster, J. C., Coster, A. J., Erickson, P. J., Holt, J. M., Lind, F. D., Rideout, W., McCready, M., van Eyken, A., Barnes, R. J., Greenwald, R. A., and Rich, F. J.: Multiradar observations of the polar tongue of ionization, J. Geophys. Res., 110, A09S31, doi:10.1029/2004JA010928, 2005.

Ghoddousi-Fard, R., Prikryl, P., and Lahaye, F.: GPS phase difference variation statistics: A comparison between phase scintillation index and proxy indices, Adv. Space Res., 52, 1397–1405, 2013.

Greenwald, R. A., Baker, K. B., Dudeney, J. R., Pinnock, M., Jones, T. B., Thomas, E. C., Villain, J.-P., Cerrisier, J.-C., Senior, C., Hanuise, C., Hunsucker, R. D., Sofko, G., Koehler, J., Nielsen, E., Pellinen, R., Walker, A. D. M., Sato, N., and Yamagishi, H.: DARN/SUPERDARN A global view of the dynamics of highlatitude convection, Space Sci. Rev., 71, 761–796, 1995.

Grocott, A., Milan, S. E., Yeoman, T. K., Sato, N., Yukimatu, A. S., and Wild, J. A.: Superposed epoch analysis of the ionospheric convection evolution during substorms: IMF BY dependence, J. Geophys. Res., 115, A00I06, doi:10.1029/2010JA015728, 2010.

Holzworth, R. H. and Meng, C.-I.: Mathematical Representation of the Auroral Oval, Geophys. Res. Lett., 2, 377–380, 1975.

Imber, S. M., Milan, S. E., and Lester, M.: The Heppner-Maynard Boundary measured by SuperDARN as a proxy for the latitude of the auroral oval, J. Geophys. Res. Space Physics, 118, 685–697, doi:10.1029/2012JA018222, 2013.

Jayachandran, P. T., Langley, R. B., MacDougall, J. W., Mushini, S. C., Pokhotelov, D., Hamza, A. M., Mann, I. R., Milling, D. K., Kale, Z. C., Chadwick, R., Kelly, T., Danskin, D. W., and Carrano, C. S.: Canadian High Arctic Ionospheric Network (CHAIN), Radio Sci., 44, RS0A03, doi:10.1029/2008RS004046, 2009.

Jiao, Y., Morton, Y. T., Taylor, S., and Pelgrum, W.: Characterization of high-latitude ionospheric scintillation of GPS signals, Radio Sci., 48, 698–708, doi:10.1002/2013RS005259, 2013.

Jin Y., Moen, J. I., and Miloch, W. J.: GPS scintillation effects associated with polar cap patches and substorm auroral activity: direct comparison, J. Space Weather Space Clim., 4, A23, doi:10.1051/swsc/2014019, 2014.

King, J. H. and Papitashvili, N. E.: Solar wind spatial scales in and comparisons of hourly Wind and ACE plasma and magnetic field data, J. Geophys. Res., 110, A02104, doi:10.1029/2004JA010649, 2005.

Kinrade, J., Mitchell, C. N., Smith, N. D., Ebihara, Y., Weatherwax, A. T., and Bust, G. S.: GPS phase scintillation associated with optical auroral emissions: First statistical results from the geographic South Pole, J. Geophys. Res. Space Physics, 118, 2490–2502, doi:10.1002/jgra.50214, 2013.

Kintner, P. M., Ledvina, B. M., and de Paula, E. R.: GPS and ionospheric scintillations, Space Weather, 5, S09003, doi:10.1029/2006SW000260, 2007.

Kokubun, S., Yamamoto, T., Acuna, M. H., Hayashi, K., Shiokawa, K., and Kawano H.: The Geotail Magnetic Field Experiment, J. Geomag. Geoelectr., 46, 7–21, 1994.

Kunduri, B. S. R., Baker, J. B. H., Ruohoniemi, J. M., Clausen, L. B. N., Grocott, A., Thomas, E. G., Freeman M. P., and Talaat E. R.: An examination of inter-hemispheric conjugacy in a subauroral polarization stream, J. Geophys. Res., 117, A08225, doi:10.1029/2012JA017784, 2012.

Liu, W. W.: Canadian space environment program and international living with a star, Adv. Space Res., 35, 51–60, 2005.

Makarevich, R. A. and Bristow, W. A.: Fine structure of subauroral electric field and electron content, J. Geophys. Res. Space Physics, 119, 3789–3802, doi:10.1002/2014JA019821, 2014.

Mann, I. R., Milling, D. K., Rae, I. J., Ozeke, L. G., Kale, A., Kale, Z. C., Murphy, K. R., Parent, A., Usanova, M., Pahud, D. M., Lee, E.-A., Amalraj, V., Wallis, D. D., Angelopoulos, V., Glassmeier, K.-H., Russell, C. T., Auster, H.-U., and Singer, H. J.: The Upgraded CARISMA Magnetometer Array in the THEMIS Era, Space Sci. Rev., 141, 413–451, 2008.

Moen, J., Oksavik, K., Alfonsi, L., Daabakk, Y., Romano, V., and Spogli, L.: Space weather challenges of the polar cap ionosphere, J. Space Weather Space Clim., 3, A02, doi:10.1051/swsc/2013025, 2013.

Newell, P. T., Liou, K., and Wilson, G. R.: Polar cap particle precipitation and aurora: Review and commentary, J. Atmos. Solar-Terr. Phys., 71, 199–215, 2009.

Nishimura, Y., Lyons, L. R., Shiokawa, K., Angelopoulos, V., Donovan, E. F., and Mende, S. B.: Substorm onset and expansion phase intensification precursors seen in polar cap patches and arcs, J. Geophys. Res. Space Physics, 118, 2034–2042, doi:10.1002/jgra.50279, 2013.

Paxton, L. J., Morrison, D., Zhang, Y., Kil, H., Wolven, B., Ogorzalek, B. S., Humm, D. C., and Meng, C.-I.: Validation of remote sensing products produced by the Special Sensor Ultraviolet Scanning Imager (SSUSI) – a far-UV imaging spectrograph on DMSP F16, Proc. SPIE, 4485, 338, 2002.

Pinnock, M., Rodger, A. S., Dudeney, J. R., Baker, K. B., Newell, P. T., Greenwald, R. A., and Greenspan, M. E.: Observations of an enhanced convection channel in the cusp ionosphere, J. Geophys. Res., 98, 3767–3776, 1993.

Prikryl, P., MacDougall, J. W., Grant, I. F., Steele, D. P., Sofko, G. J., and Greenwald, R. A.: Observations of polar patches generated by solar wind Alfvén wave coupling to the dayside magnetosphere, Ann. Geophys., 17, 463–489, doi:10.1007/s00585-999-0463-0, 1999.

Prikryl, P., Jayachandran, P. T., Mushini, S. C., and Chadwick, R.: Climatology of GPS phase scintillation and HF radar backscatter for the high-latitude ionosphere under solar minimum conditions, Ann. Geophys., 29, 377–392, doi:10.5194/angeo-29-377-2011, 2011.

Prikryl, P., Zhang, Y., Ebihara, Y., Ghoddousi-Fard, R., Jayachandran, P. T., Kinrade, J., Mitchell, C. N., Weatherwax, A. T., Bust, G., Cilliers, P. J., Spogli, L., Alfonsi, L., De Franceschi, G., Romano, V., Ning, B., Li, G., Jarvis, M. J., Danskin, D. W., Spanswick, E., Donovan, E., and Terkildsen, M.: An interhemispheric comparison of GPS phase scintillation with auroral emission observed at South Pole and from DMSP satellite, Special Issue of Annals of Geophysics, 56, 2, R0216; doi:10.4401/ag-6227, 2013a.

Prikryl, P., Ghoddousi-Fard, R., Kunduri, B. S. R., Thomas, E. G., Coster, A. J., Jayachandran, P. T., Spanswick, E., and Danskin, D. W.: GPS phase scintillation and proxy index at high latitudes during a moderate geomagnetic storm, Ann. Geophys., 31, 805–816, doi:10.5194/angeo-31-805-2013, 2013b.

Prikryl ,P., Ghoddousi-Fard, R., Spogli, L., Mitchell, C. N., Li, G., Ning, B., Cilliers, P. J., Sreeja, V., Aquino, M., Terkildsen, M., Jayachandran, P. T., Jiao, Y., Morton, Y. T., Ruohoniemi, J. M., Thomas, E. G., Zhang, Y., Weatherwax, A. T., Alfonsi, L., De Franceschi, G., and Romano, V.: GPS phase scintillation at high latitudes during geomagnetic storms of 7–17 March 2012 – Part 2: Interhemispheric comparison, Ann. Geophys., 33, 657–670, doi:10.5194/angeo-33-657-2015, 2015a.

Prikryl, P., Ghoddousi-Fard, R., Ruohoniemi, J. M., and Thomas, E. G.: GPS phase scintillation at high latitudes during two geomagnetic storms, in: Auroral dynamics and space weather, edited by: Zhang, Y. and Paxton, L. J. , AGU, Wiley Publ., accepted, 2015b.

Rideout, W. and Coster, A.: Automated GPS processing for global total electron content data, GPS Solutions, 10, 219–228, 2006.

Ruohoniemi, J. M. and Greenwald, R. A.: Dependencies of highlatitude plasma convection: Consideration of interplanetary magnetic field, seasonal, and universal time factors in statistical patterns, J. Geophys. Res., 110, A09204, doi:10.1029/2004JA010815, 2005.

Shepherd, S. G.: Altitude-adjusted corrected geomagnetic coordinates: Definition and functional approximations, J. Geophys. Res. Space Physics, 119, 7501–7521, doi:10.1002/2014JA020264, 2014.

Spogli, L., Alfonsi, L., De Franceschi, G., Romano, V., Aquino, M. H. O., and Dodson, A.: Climatology of GPS ionospheric scintillations over high and mid-latitude European regions, Ann. Geophys., 27, 3429–3437, doi:10.5194/angeo-27-3429-2009, 2009.

Thomas, E. G., Baker, J. B. H., Ruohoniemi, J. M., Clausen, L. B. N., Coster, A. J., Foster, J. C., and Erickson P. J.: Direct observations of the role of convection electric field in the formation of a polar tongue of ionization from storm enhanced density, J. Geophys. Res. Space Physics, 118, 1180–1189, doi:10.1002/jgra.50116, 2013.

Tiwari, R., Ghafoori, F., Al-Fanek, O., Haddad, O., Skone, S., "Investigation of High Latitude Ionospheric Scintillations Observed in the Canadian Region", Proceedings of the 23rd International Technical Meeting of The Satellite Division of the Institute of Navigation (ION GNSS 2010), Portland, OR, 349–360, September 2010.

Tsurutani, B. T., Judge, D. L., Guarnieri, F. L., P. Gangopadhyay, Jones, A. R., Nuttall, J., Zambon, G. A., Didkovsky, L., Mannucci, A. J., Iijima, B., Meier, R. R., Immel, T. J., Woods, T. N., Prasad, S., Floyd, L., Huba, J., Solomon, S. C., Straus, P., and Viereck, R.: The October 28, 2003 extreme EUV solar flare and resultant extreme ionospheric effects: Comparison to other Halloween events and the Bastille Day event, Geophys. Res. Lett., 32, L03S09, doi:10.1029/2004GL021475, 2005.

Tsurutani, B. T., Echer, E., Shibata, K., Verkhoglyadova, O. P., Mannucci, A. J., Gonzalez, W. D., Kozyra, J. U., and Pätzold, M.: The interplanetary causes of geomagnetic activity during the 7–17 March 2012 interval: a CAWSES II overview, J. Space Weather Space Clim. 4, A02, doi:10.1051/swsc/2013056, 2014.

van der Meeren, C., Oksavik, K., Lorentzen, D., Moen, J. I., and Romano, V.: GPS scintillation and irregularities at the front of an ionization tongue in the nightside polar ionosphere, J. Geophys Res. Space Physics, 119, 8624–8636, doi:10.1002/2014JA020114, 2014.

Van Dierendonck, A. J. and Arbesser-Rastburg, B.: Measuring ionospheric scintillation in the equatorial region over Africa, including measurements from SBAS geostationary satellite signals, Proceeding of ION GNSS 17th technical meeting of the satellite division, Long Beach, CA, 316–324, 21–24 September 2004.

Zhang, Q.-H., Zhang, B.-C., Liu, R.-Y., Dunlop, M. W., Lockwood, M., Moen, J., Yang, H.-G., Hu, H.-Q., Hu, Z.-J., Liu, S.-L., McCrea, I. W., and Lester, M.: On the importance of interplanetary magnetic field |By| on polar cap patch formation, J. Geophys. Res., 116, A05308, doi:10.1029/2010JA016287, 2011.

Zhang, Y. and Paxton, L. J.: An empirical Kp-dependent global auroral model based on TIMED/GUVI FUV data, J. Atmosph. Solar-Terrest. Phys., 70, 1231–1242, 2008.

Zou, Y., Nishimura, Y., Lyons, L. R., Donovan, E. F., Ruohoniemi, J. M., Nishitani, N., and McWilliams, K. A.: Statistical relationships between enhanced polar cap flows and PBIs, J. Geophys. Res. Space Physics, 119, 151–162, doi:10.1002/2013JA019269, 2014.